Interferometric synthetic aperture radar study of Okmok volcano, Alaska, 1992–2003: Magma supply dynamics and postemplacement lava flow deformation

Zhong Lu and Timothy Masterlark

Science Applications International Corporation, National Center for Earth Resources Observation and Research, U.S. Geological Survey, Sioux Falls, South Dakota, USA

Daniel Dzurisin

U.S. Geological Survey, David A. Johnston Cascades Volcano Observatory, Vancouver, Washington, USA

Received 20 April 2004; revised 19 November 2004; accepted 6 December 2004; published 23 February 2005.

[1] Okmok volcano, located in the central Aleutian arc, Alaska, is a dominantly basaltic complex topped with a 10-km-wide caldera that formed circa 2.05 ka. Okmok erupted several times during the 20th century, most recently in 1997; eruptions in 1945, 1958, and 1997 produced lava flows within the caldera. We used 80 interferometric synthetic aperture radar (InSAR) images (interferograms) to study transient deformation of the volcano before, during, and after the 1997 eruption. Point source models suggest that a magma reservoir at a depth of 3.2 km below sea level, located beneath the center of the caldera and about 5 km northeast of the 1997 vent, is responsible for observed volcano-wide deformation. The preeruption uplift rate decreased from about 10 cm yr^{-1} during 1992–1993 to 2 $\sim$ 3 cm yr^{-1} during 1993–1995 and then to about $-1 \sim -2$ cm yr^{-1} during 1995–1996. The posteruption inflation rate generally decreased with time during 1997–2001, but increased significantly during 2001–2003. By the summer of 2003, 30 $\sim$ 60% of the magma volume lost from the reservoir in the 1997 eruption had been replenished. Interferograms for periods before the 1997 eruption indicate consistent subsidence of the surface of the 1958 lava flows, most likely due to thermal contraction. Interferograms for periods after the eruption suggest at least four distinct deformation processes: (1) volcano-wide inflation due to replenishment of the shallow magma reservoir, (2) subsidence of the 1997 lava flows, most likely due to thermal contraction, (3) deformation of the 1958 lava flows due to loading by the 1997 flows, and (4) continuing subsidence of 1958 lava flows buried beneath 1997 flows. Our results provide insights into the postemplacement behavior of lava flows and have cautionary implications for the interpretation of inflation patterns at active volcanoes.

Citation: Lu, Z., T. Masterlark, and D. Dzurisin (2005), Interferometric synthetic aperture radar study of Okmok volcano, Alaska, 1992–2003: Magma supply dynamics and postemplacement lava flow deformation, *J. Geophys. Res.*, *110*, B02403, doi:10.1029/2004JB003148.

1. Introduction

[2] Okmok is a dominantly basaltic central volcanic complex that occupies most of the northeastern end of Umnak Island, Alaska (Figure 1). Catastrophic pyroclastic eruptions circa 12.0 and 2.05 ka resulted in the formation of two overlapping summit calderas [*Byers*, 1959]. Subsequent eruptions produced a field of small cones and lava flows, including several historically active vents within the younger caldera [*Grey*, 2003; *Miller et al.*, 1998]. Most of the volcano's historical eruptions are poorly documented owing to its remote location. Minor explosive eruptions occurred in 1931, 1936, 1938, 1943, 1960–1961, 1981, 1983, and 1986–1988; blocky basaltic flows were extruded during relatively large effusive eruptions in 1945, 1958 and 1997 [*Grey*, 2003; *McGimsey and Wallace*, 1999; *Miller et al.*, 1998]. All of these eruptions originated from Cone A, located on the southern edge of the caldera floor (Figure 1), which formed almost entirely during the 20th century [*Grey*, 2003].

[3] A 6.5-km-long lava flow issued from a fissure near the southwest base of Cone A in 1945 (Figure 1) [*Grey*, 2003; *Miller et al.*, 1998]. The average thickness of the 1945 flow is 12 m and its volume is $1 \sim 2 \times 10^7$ m^3 [*Byers et al.*, 1947; *Bulletin of Volcanic Eruptions* (BVE), 1984]. As a result of the 1945 eruption, Cone A increased about 30 m in height and developed a broad central crater. During the 1958 eruption, a′a′ and pahoehoe flows from a fissure near the northeast base of Cone A extended as far as 8 km

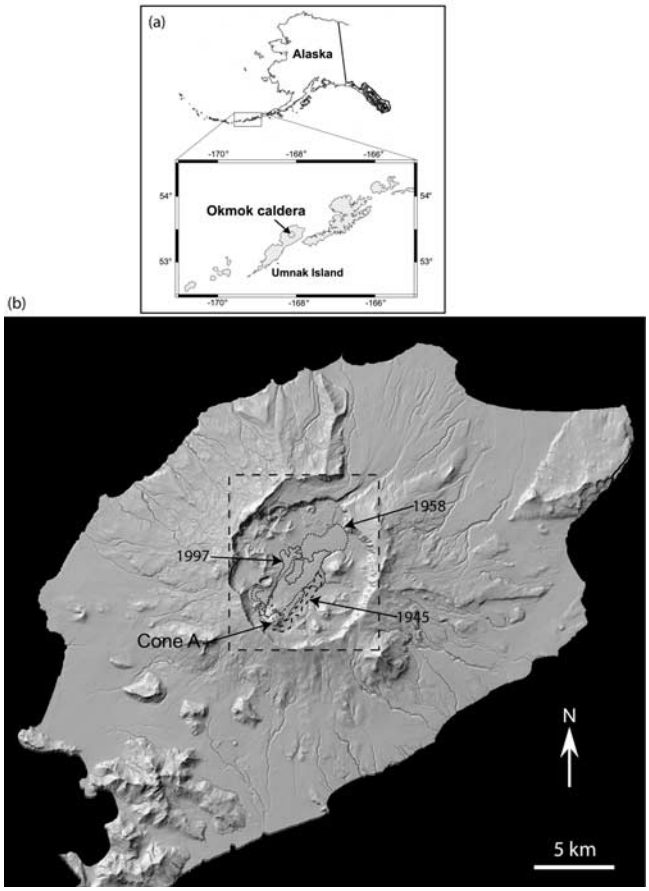

Figure 1. (a) Map of Alaska showing the 2500-km-long Aleutian volcanic arc and Umnak Island (inset), where Okmok volcano is located. (b) Shaded relief image of Okmok volcano, with outlines marking the extents of lava flows from eruptions in 1945, 1958, and 1997. The 1997 flows overrode parts of the 1945 flows and most of the 1958 flows. The dashed rectangle shows the location and area covered by Figures 10–12.

across the caldera floor and impounded a lake against the far caldera wall (Figure 1) [*Grey*, 2003]. The average thickness of the 1958 flows is 13 m, but in places they are as much as 20 $\sim$ 30 m thick. With an estimated volume of 10^8 m^3, they cover an area of about 9.4 km^2 (BVE, 1984). The most recent eruption of Okmok, a moderate Hawaiian to Strombolian type with an ash plume that reached 10 km altitude, began in early February 1997 and ended in late April 1997 [*Miller et al.*, 1998; *Patrick et al.*, 2003]. The 1997 lava flows traveled about 6 km, partly overriding the 1958 flows, and are generally similar to the a'a' flows from previous eruptions.

[4] Remote sensing played an essential role in documenting the 1997 eruption at this remote and poorly instrumented volcano [*Dean et al.*, 1998; *Lu et al.*, 1998, 2000a, 2003a; *Mann et al.*, 2002; *Patrick et al.*, 2003]. AVHRR nighttime images acquired between February and April 1997 were used to characterize the eruptive activity [*Patrick et al.*, 2003]. On the basis of Landsat ETM+ imagery and field investigations, the 1997 lava covers an area of 8.9 km^2 [*Lu et al.*, 2003a; *Patrick et al.*, 2003]. Digital elevation models (DEMs) that represent the caldera topography before and after the 1997 eruption were produced using multiple ERS-1 and ERS-2 radar satellite interferograms and airborne AIRSAR interferometric data sets. The thickness of the 1997 flows was mapped by differencing preeruption and posteruption DEMs: the average and maximum thicknesses of the flows are 17 m and 50 m, respectively [*Lu et al.*, 2003a].

[5] Deformation associated with the February–April 1997 Okmok eruption derived from interferometric synthetic aperture radar (InSAR) observations was first reported by *Lu et al.* [1998]. The central part of the caldera floor rose about 20 cm during 1992–1995 (prior to the eruption) and subsided about 1.4 m during 1995–1997. Presumably, preeruption uplift was caused by accumulation of magma within a shallow reservoir beneath the caldera and subsidence resulted from withdrawal of the magma that fed the eruption. *Lu et al.* [2000a] and *Mann et al.* [2002] used a dozen additional ERS-1 and ERS-2 interferograms to analyze and model deformation during 1992–1995, 1995–1997, and 1997–1998. For this paper, we produced 80 interferograms from 88 radar images of Okmok acquired during 1992–2003. The images are from four different sensors (ERS-1, ERS-2, RADARSAT-1, and JERS-1 satellites) operating at two different wavelengths (C band and L band), with a total of 10 different viewing geometries. We systematically modeled the interferograms, conducted least squares inversion of transient deformation, and analyzed residual interferograms to infer postemplacement lava flow deformation. Compared with previous InSAR results for Okmok [*Lu et al.*, 1998, 2000a; *Mann et al.*, 2002], this paper makes the following advances:

[6] 1. Previous studies utilized a relatively small number of SAR images from ERS-1 and ERS-2, whereas for this paper we produced 80 interferograms using 88 ERS-1, ERS-2, RADARSAT-1 (C band, λ = 5.66 cm), and JERS-1 (L band, λ = 23.53 cm) images. The interferograms used for the previous studies covered only the periods 1992–1993, 1993–1995, 1995–1997, and 1997–1998; this paper includes interferograms for nearly every yearly interval from 1992 to 2003. A new 1995–1996 interferogram, for example, further constrained transient deformation before the February–April 1997 eruption. Furthermore, the 80 interferograms were constructed from a total of 10 different viewing geometries, using both descending and ascending satellite passes. Multiple interferograms span numerous intervals and all interferograms together were used to characterize transient deformation during 1992–2003. To the best of our knowledge, this is the first paper that studies one volcano using a combination of multiple satellite systems of two wavelengths with a variety of viewing geometries.

[7] 2. In this paper, parameter optimization of deformation source models is based on a nonlinear least squares inversion approach, which also takes into account topographic departures from the half-space assumption [*Williams and Wadge*, 1998].

[8] 3. We inverted all 80 interferograms for subsurface volume changes to estimate annual magma flux using a least squares approach [*Berardino et al.*, 2002; *Usai*, 2003; *Schmidt and Burgmann*, 2003]. This reduces the effect of atmosphere anomalies on the estimated volume changes and greatly facilitates the interpretation of transient deformation.

Table 1. SAR Images Used for This Study[a]

	Image 1				Image 2								
ID	Orbit	Year	Month	Day	Orbit	Year	Month	Day	Track	$\mathbf{B_n}$, m	$\Delta\mathbf{V}$, m^3	RMSE, mm	Figure
0	105878	1992	8	30	120250	1995	5	30	222	−22			4a
1	106773	1992	10	31	112284	1993	11	20	115	13	7.65E+06[b]	12.7	2a
2	109779	1993	5	29	110280	1993	7	3	115	−159			
3	110509	1993	7	19	111010	1993	8	23	344	2			6a
4	110738	1993	8	4	121603	1995	9	1	72	−154	3.55E+06	9.7	2b, 10a
5	110738	1993	8	4	207441	1996	9	27	72	−136	2.46E+06	8.2	4b, 10i
6	110781	1993	8	7	122147	1995	10	9	115	304	3.71E+06	8.0	2c, 10b
7	111239	1993	9	8	122104	1995	10	6	72	−230	2.99E+06	9.2	10c
8	111282	1993	9	11	122147	1995	10	9	115	−97	2.97E+06	10.0	10d
9	111740	1993	10	13	122104	1995	10	6	72	−24	2.33E+06	8.2	10e
10	111740	1993	10	13	207441	1996	9	27	72	−339	2.32E+06	10.1	
11	111783	1993	10	16	122147	1995	10	9	115	−72	2.08E+06	7.8	10f
12	112012	1993	11	1	122376	1995	10	25	344	71	1.95E+06	5.4	10g
13	112012	1993	11	1	202703	1995	10	26	344	154	1.65E+06	6. 1	10h
14	121603	1995	9	1	207441	1996	9	27	72	18	−1.34E+06	4.5	2d, 10j
15	122104	1995	10	6	203433	1995	12	16	72	4			6b
16	124108	1996	2	3	207942	1996	10	26	72	10			6c
17	120372	1995	6	7	122877	1995	11	29	344	−170			
18	210218	1997	4	3	213725	1997	12	14	344	−2			6d
19	210719	1997	5	8	211721	1997	7	17	344	98			6e
20	210719	1997	5	8	212723	1997	9	25	344	75			6f
21	210719	1997	5	8	217733	1998	9	10	344	167	7.11E+06	5.1	
22	211492	1997	7	1	217504	1998	8	25	115	236	5.62E+06	7.2	
23	211492	1997	7	1	222013	1999	7	6	115	−119	8.52E+06	7.1	4c
24	211492	1997	7	1	227524	2000	7	25	115	−72	1.05E+07	2	
25	211721	1997	7	17	217733	1998	9	10	344	69	5.70E+06	4.4	2h
26	211721	1997	7	17	221741	1999	6	17	344	48	6.77E+06	10.5	
27	211721	1997	7	17	228254	2000	9	14	344	−41	1.26E+07	11.7	4d
28	212494	1997	9	9	218005	1998	9	29	115	190	4.82E+06	8.7	2i
29	212494	1997	9	9	228025	2000	8	29	115	−80	1.17E+07	9.4	4e
30	212723	1997	9	25	217733	1998	9	10	344	92	3.88E+06	3.7	2j, 11a
31	212723	1997	9	25	221741	1999	6	17	344	−25	6.92E+06	5.1	
32	212723	1997	9	25	228254	2000	9	14	344	−18	1.20E+07	9.2	4f
33	216731	1998	7	2	222743	1999	8	26	344	−251	3.21E+06	8.5	3a, 11b
34	217504	1998	8	25	228526	2000	10	3	115	−11	7.98E+06	7.4	
35	217733	1998	9	10	223244	1999	9	30	344	295	4.10E+06	7.4	3b
36	217733	1998	9	10	228254	2000	9	14	344	−110	7.97E+06	8.2	
37	217733	1998	9	10	238274	2002	8	15	344	216	1.05E+07	15.2	
38	218005	1998	9	29	221512	1999	6	1	115	77	1.72E+06	6.4	
39	218005	1998	9	29	228025	2000	8	29	115	−270	6.55E+06	10.4	4g
40	218005	1998	9	29	229027	2000	11	7	115	−147	6.70E+06	11.6	
41	218005	1998	9	29	232534	2001	7	10	115	120	7.90E+06	5.6	5a
42	218005	1998	9	29	239047	2002	10	8	115	56	1.25E+07	7.1	5b
43	218463	1998	10	31	233493	2001	9	15	72	−11	6.29E+06	14.4	5c
44	218506	1998	11	3	232534	2001	7	10	115	−90	6.80E+06	5.3	
45	221741	1999	6	17	223745	1999	11	4	344	22			6h
46	221741	1999	6	17	227252	2000	7	6	344	−217	3.96E+06	8.3	
47	221741	1999	6	17	228254	2000	9	14	344	7	5.16E+06	7.5	3c
48	222013	1999	7	6	227524	2000	7	25	115	47	3.31E+06	5.9	3d
49	222471	1999	8	7	233493	2001	9	15	72	−283	4.79E+06	8.4	5d
50	222850	1999	9	3	227860	2000	8	18	451	108	3.39E+06	7.2	11c
51	223015	1999	9	14	227524	2000	7	25	115	274	3.16E+06	4.9	3e
52	223244	1999	9	30	238274	2002	8	15	344	−79	8.21E+06	5.6	5e
53	223244	1999	9	30	238775	2002	9	19	344	33	8.84E+06	7.6	5f
54	227252	2000	7	6	228254	2000	9	14	344	224			6i
55	227252	2000	7	6	237773	2002	7	11	344	−187	4.54E+06	5.6	
56	227982	2000	8	26	233493	2001	9	15	72	402	1.94E+06	6.8	3f
57	227982	2000	8	26	239004	2002	10	5	72	75	7.20E+06	7.0	
58	229027	2000	11	7	239047	2002	10	8	115	203	6.33E+06	10.2	5g
59	232534	2001	7	10	237544	2002	6	25	115	−183	3.48E+06	9.8	3h
60	232534	2001	7	10	239047	2002	10	8	115	−64	5.00E+06	5.6	3i
61	233493	2001	9	15	239505	2002	11	9	72	93	4.90E+06	12.1	3j, 11e
62	237608	2002	6	30	238610	2002	9	8	179	136			6j
63	237544	2002	6	25	239548	2002	11	12	115	52			
64	238274	2002	8	15	238775	2002	9	19	344	112			6k
65	227860	2000	8	18	237880	2002	7	19	451	8	4.01E+06	4.3	5h
66*	122147	1995	10	9	212494	1997	9	9	115	8	−4.82E+07	9.8	2e
67*	122147	1995	10	9	212494	1997	9	9	115	8	−4.73E+07	8.7	
68	325570	2000	9	27	330372	2001	8	29	800	−118	267974	5.8	3g, 11d
69	325077	2000	8	24	329536	2001	7	2	900	−9			
70	325420	2000	9	17	330222	2001	8	19	900	362	538785	7.7	
71	325420	2000	9	17	330565	2001	9	12	900	350	955053	8.9	

Table 1. (continued)

	Image 1				Image 2								
ID	Orbit	Year	Month	Day	Orbit	Year	Month	Day	Track	$\mathbf{B_n}$, m	$\Delta\mathbf{V}$, m^3	RMSE, mm	Figure
72	229027	2000	11	7	232534	2001	7	10	115	−267			
73	121646	1995	9	4	211492	1997	7	1	115	−89			2f
74	403682	1992	10	13	435314	1998	7	26	777	240	−3.39E+07	10.2	2g
75	429398	1997	6	26	430716	1997	9	22	888	692			12a
76	430042	1997	8	8	430701	1997	9	21	777	−456			12b
77	335367	2002	8	14	340855	2003	9	2	900	104	7.65E+06	9.7	3k
78	335710	2002	9	7	341198	2003	9	26	900	−156	7.52E+06	8.7	3l
79	218005	1998	9	29	218506	1998	11	3	115	210			6g

[a]Dates are image acquisition times. Orbit numbers include the satellite ID (1, ERS-1; 2, ERS-2; 3, RADARSAT-1; and 4, JERS-1) and orbit on which the images were acquired. The same track number applies to both images in an InSAR pair. $\mathbf{B_n}$ is the perpendicular component of the baseline with respect to the SAR look angle. $\Delta\mathbf{V}$ is the volume change of the source of the best fitting model in the case that the model source in three dimensions was fixed. RMSE is the root-mean-square error between the observed and modeled interferograms. Interferograms 66 and 67 are from the same, original interferogram. Phase values in the original interferogram, however, are discontinuous between two major patches which are represented by interferograms 66 and 67, respectively. So, interferograms 66 and 67 are treated as two different images.

[b]Read 7.65E + 06 as 7.65×10^6.

[9] 4. We invoked two-dimensional finite element models (FEMs) to identity possible mechanisms for postemplacement deformation of the 1958 and 1997 lava flows.

2. InSAR Observations

[10] We obtained 88 ERS-1, ERS-2, RADARSAT-1 and JERS-1 SAR images that are suitable for measuring surface deformation at Okmok (Table 1), and used the two-pass InSAR approach [e.g., *Massonnet and Feigl*, 1998; *Rosen et al.*, 2000] to produce 80 deformation interferograms with reasonably good coherence. The digital elevation model (DEM) used to produce the interferograms was derived from the NASA TOPSAR system, with a pixel spacing of 5 meters and vertical error of less than 10 m [*Madsen et al.*, 1995; *Lu et al.*, 2003a]. For each image pair, we optimized the Doppler centroid during SAR image generation. The average Doppler centroid of the two images was used to process the SAR signal data into single-look complex images from which the interferograms were produced [*Gatelli et al.*, 1994]. To refine baseline estimations, we used the precision state vectors for ERS-1 and ERS-2 satellites [*Massmann*, 1995; *Scharroo and Visser*, 1998]. Because the accuracy of the satellite state vectors provided in JERS-1 or RADARSAT-1 metadata is not as good as that for ERS-1 and ERS-2, we refined baselines of JERS-1 and Radarsast-1 interferograms by using known elevations from the DEM and applying a least squares approach [*Rosen et al.*, 1996].

[11] The SAR images were acquired in 10 different imaging modes during both descending and ascending passes (Table 2). The satellites travel from about N10°E to S10°W for the descending passes, and the SAR sensors are directed ∼N80°W with look angles of 20.8° ∼ 46.0° from vertical. In ascending passes, the satellites travel from about S10°E to N10°W with look angles of 19.6° and 44.3°, respectively. The line of sight (LOS) vectors for the SAR images used in this study, defined as [east, north, up], are given in Table 2. For Aleutian volcanoes, interferometric coherence is maintained only in summer images [*Lu and Freymuller*, 1998]. Therefore most of the images in Table 1 span 1 year or multiple years. Useful data for interferometry were not acquired in the summer of 1994; therefore no interferograms start or end in that year.

[12] Figures 2 and 3 show a few examples of interferograms with temporal separation of 1 year, plus two 1993–1995 interferograms and one 1992–1998 interferogram. Together, these images map patterns of deformation before, during, and after the eruption, and lead to the following observations:

[13] 1. More than 5 fringes appear inside the caldera in the 1992–1993 interferogram (Figure 2a), but only 2 fringes appear in the 1993–1995 interferograms (Figures 2b–2c). We infer that the center of the caldera rose more than 14 cm during 1992–1993 and about 6 cm during 1993–1995. The 1995–1996 interferogram (Figure 2d) suggests that the caldera subsided 1 ∼ 2 cm during the time interval from 1.5 to 0.5 years before the 1997 eruption. Therefore the preeruption inflation rate decreased with time during 1992–1995 and inflation stopped sometime during 1995–1996.

[14] 2. Interferometric coherence is better and persists longer at L band than at C band, confirming conclusions from InSAR investigations at other places [e.g., *Rosen et al.*, 1996; *Murakami et al.*, 1996; *Lu et al.*, 2005]. For example, the coherence of the 1992–1998 L band interferogram (which only covers the eastern two thirds of Okmok volcano) (Figure 2g) is slightly higher than that of 1995–1997 C band interferograms (Figures 2e and 2f).

[15] 3. The posteruption inflation rate generally decreased with time during 1997–2001. However, the inflation rate increased again during 2001–2003 to a value greater than that for 1997–1998. The inflation rate during 2002–2003 is the highest observed since the 1997 eruption.

Table 2. Line-of-Sight (LOS) Vectors for the 10 Different Satellite Tracks Listed in Table 1

Track	LOS Vector [East, North, Up]
222	[−0.411, −0.097, 0.906]
115	[0.346, −0.081, 0.935]
344	[0.385, −0.091, 0.918]
72	[0.579, −0.137, 0.804]
451	[−0.377, −0.089, 0.922]
179	[−0.326, −0.077, 0.942]
800	[0.711, −0.111, 0.695]
900	[−0.690, −0.108, 0.716]
777	[−0.638, −0.115, 0.762]
888	[−0.618, −0.111, 0.778]

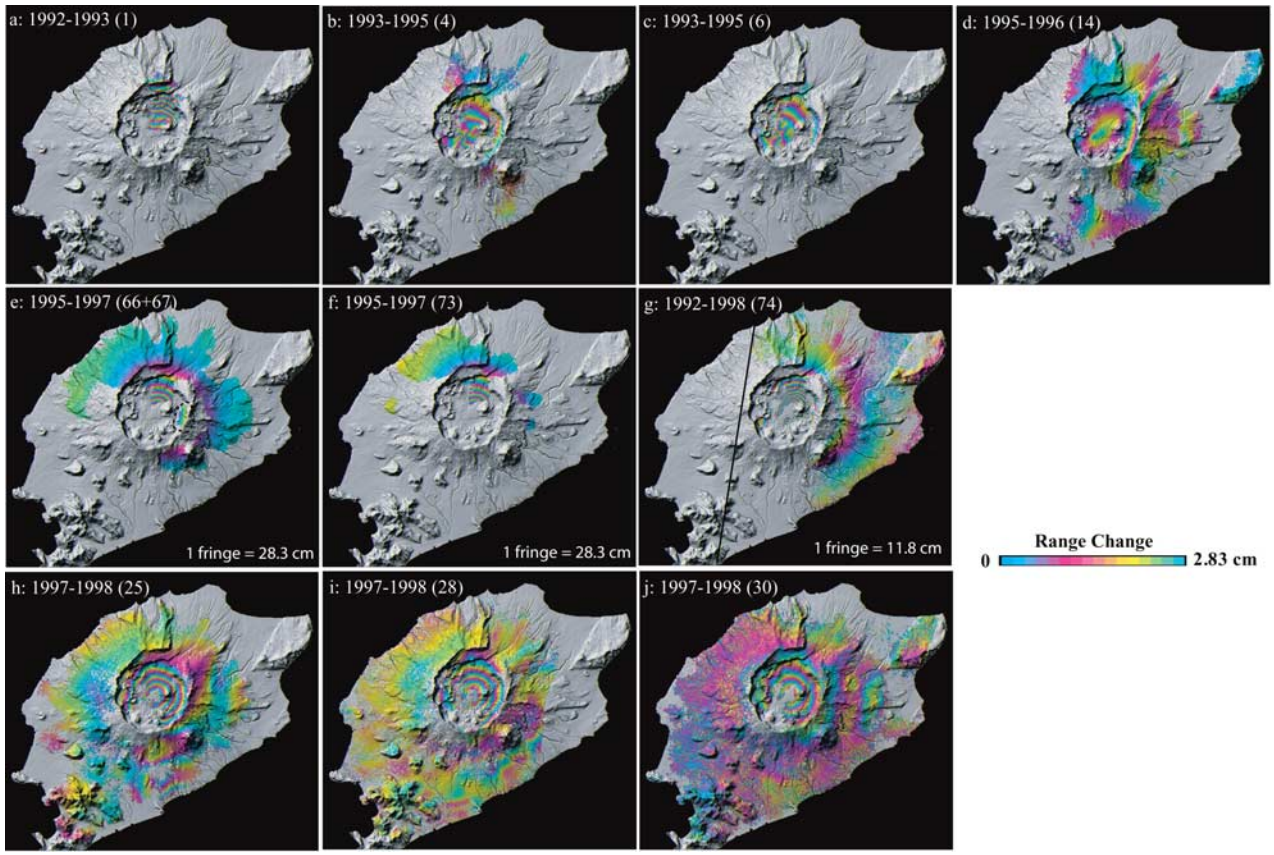

Figure 2. Examples of interferograms showing deformation of Okmok volcano for various time periods during 1992–1998. Each fringe (full color cycle) represents 2.83 cm of range change between the ground and the satellite, unless noted otherwise (Figures 2e, 2f, and 2g). Additional information on SAR images used to produce the interferograms is given in Table 1. Each interferogram covers the same area as Figure 1b. The time interval and identification number (in parentheses, see Table 1) of each interferogram are labeled. Areas that lack interferometric coherence are uncolored. Figure 2e is composed of interferogram 66 and interferogram 67 that is outlined by the dash line (see Table 1 for details). The dark line in Figure 2g marks the western edge of JERS-1 SAR images.

[16] 4. Post-1997 interferograms reveal both volcano-wide and localized deformation (see, for example, Figures 3f–3i), presumably caused by two or more mechanisms. We assume one mechanism is inflation caused by magma injection into a shallow reservoir and a second is postemplacement deformation related to the 1997 lava flows. Similarly, localized deformation associated with the 1958 lava flows is observed in the 1993–1995 interferograms (Figures 2b–2c).

[17] Figures 4 and 5 show a few examples of interferograms for time intervals of 2, 3, or 4 years, which are consistent with the observations enumerated above. Figure 6 shows examples of interferograms for intervals of a few months. The following inferences are based on the full suite of interferograms shown in Figures 2–6:

[18] 1. Preeruptive and posteruptive deformation occurred progressively over periods of a few years. The average deformation rate from interferograms with time intervals of a few months (Figure 6) is generally consistent with that from 1-year or multiyear interferograms (Figures 2–5). This indicates that the deformation did not happen in a matter of hours, days, or months, but instead spanned a year or more.

[19] 2. Interferogram in Figure 6c confirms that the center of the caldera subsided slightly during 1995–1996 (Figure 2d). Only a few SAR images suitable for interferometry were acquired in 1996. These limited number of interferograms prove vital in deducing the noninflation of the caldera during the period from 1.5 to 0.5 years before the start of the 1997 eruption.

[20] 3. Inflation resumed shortly after the 1997 eruption ended. Interferograms in Figures 6e and 6f show that the center of the caldera rose about 3 cm in 70 days from 8 May to 17 July 1997, and about 6 cm in 140 days from 8 May to 25 September 1997. This suggests that magma from greater depth started to replenish the shallow reservoir as soon as the eruption ended.

[21] Inspection of the Okmok interferograms, which span time periods ranging from several months during the subarctic summer to a few years between summers, leads us to the following conclusions concerning the persistence of radar interferometric coherence:

[22] 1. Coherence within the caldera is maintained as much as 4 years at C band and 6 years at L band if the images are acquired during summer or early fall.

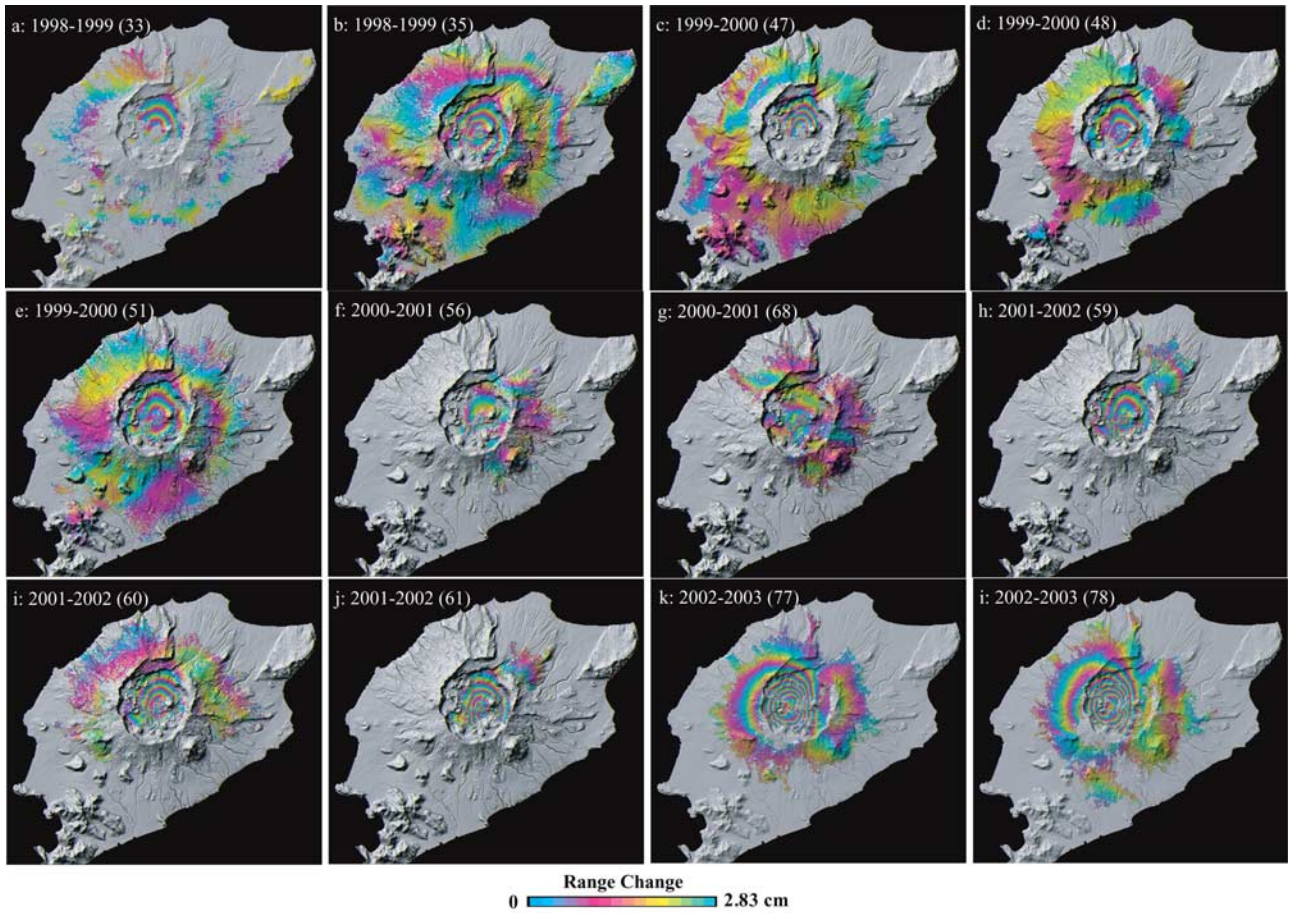

Figure 3. Examples of interferograms showing progressive reinflation of Okmok volcano after its 1997 eruption. Each interferogram spans a time interval of about 1-year. Each fringe (full color cycle) represents 2.83 cm of range change between the ground and the satellite. Additional information on SAR images used to produce the interferograms is given in Table 1. Areas that lack interferometric coherence are uncolored.

[23] 2. Coherence inside the caldera is higher than that outside the caldera. Furthermore, coherence inside the caldera does not decrease significantly with time, whereas coherence outside the caldera decreases dramatically with time. The blocky lava flows covering the caldera floor have high coherence. The relatively loose, tephra-rich material covering the volcano's flanks [*Grey*, 2003] has low coherence. *Lu and Freymueller* [1998] made similar observations on other Aleutian volcanoes.

[24] 3. The degree of coherence strongly depends on the image acquisition time. The best coherence comes from images collected during August and September. Snow and ice cover, which contributes significantly to poor coherence, is minimal during these months at Okmok.

[25] Some of the interferograms in Figures 2–6 seem to be contaminated by atmospheric delay anomalies, which can be severe in the Aleutian environment [*Lu et al.*, 2000a, 2003b]. The atmospheric artifacts are particularly problematic for the interferograms that span a few months (Figure 6). This is because real range changes due to volcanic deformation during short intervals are usually smaller than the apparent range changes due to atmospheric effects. Inspection reveals two types of atmospheric artifacts. One type is correlated with topography [*Beauducel et al.*, 2000] and the other is not. For example, fringes in the western and northwestern portions of Figure 6a, and those in the southeastern part of Figure 6e, are not correlated with topography. On the other hand, the atmospheric artifacts in Figure 6k correlate well with topography. The latter artifacts cannot be caused by DEM errors, because the baseline is short enough relative to the accuracy of the DEM to preclude this possibility. Instead, the topography-correlated artifacts are probably caused by quasi-stable concentrations of water vapor that are set up by topography. Atmospheric anomalies tend to bias the estimate of deformation source parameters and consequently the time series analysis of deformation behavior. Such artifacts are not correlated in time and their effects can be reduced if multiple interferograms are used [*Zebker et al.*, 1997].

3. Modeling and Interpretation of Volcano-wide Deformation

[26] We first modeled the interferograms to study volcano-wide deformation related to magma injection or extrusion. Our goal was to characterize the deformation

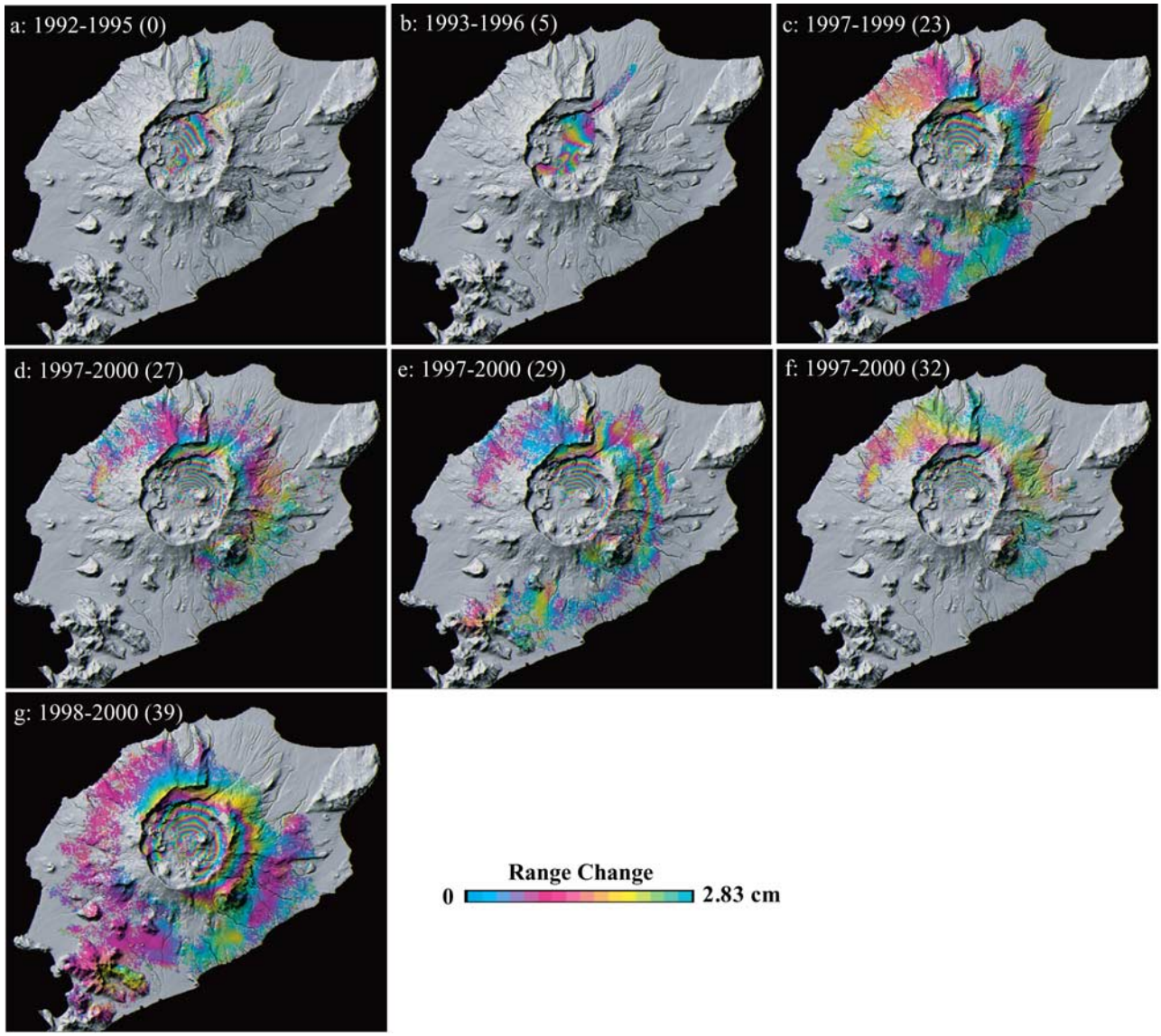

Figure 4. Examples of interferograms showing multiyear deformation of Okmok volcano before and after the 1997 eruption. Each fringe (full color cycle) represents 2.83 cm of range change between the ground and the satellite. Additional information on SAR images used to produce the interferograms is given in Table 1. Areas that lack interferometric coherence are uncolored.

rate as a function of time based on interferograms that collectively span 11 years, including preeruptive, coeruptive, and posteruptive periods (Table 1 and Figures 2–6). On the basis of the shape and radial pattern of the displacement field, we assumed that deformation was caused by a volume change in a spherical magma reservoir, and modeled the surface displacement field using a "tension sphere" source within a homogenous isotropic elastic half-space [*McCann and Wilts*, 1951; *Mogi*, 1958].

[27] Similar to the modeling scheme used for Westdahl volcano [*Lu et al.*, 2003b], we defined a Cartesian coordinate system with east, north and up axes having an origin collocated with the top, left (northwest) corner of the interferograms. The predicted LOS displacement (u) at the free surface (x_1, x_2, 0) of a homogeneous isotropic elastic half-space due to a change in the volume (ΔV) of a sphere (i.e., a presumed magma reservoir) can be expressed as follows:

$$u(x_1 - x_1', x_2 - x_2', 0) = \Delta V \frac{(1-\nu)(1+\nu)}{2\pi(1-2\nu)} \frac{x_i - x_i'}{R^3} n_i \quad (1)$$

where x_1', x_2', and $-x_3'$ are the horizontal locations and depth of the center of the sphere, R is the distance between the sphere and the displacement location, ν is the Poisson's ratio of the host rock, and n_i is the satellite LOS vector (Table 2).

[28] As mentioned above, the amount of ground deformation in interferograms spanning just a few months can be significantly less than the magnitude of atmospheric artifacts (Figure 6). Therefore we used a total of 63 interferograms spanning at least one year for this phase of the modeling. Four of the 63 interferograms could not be

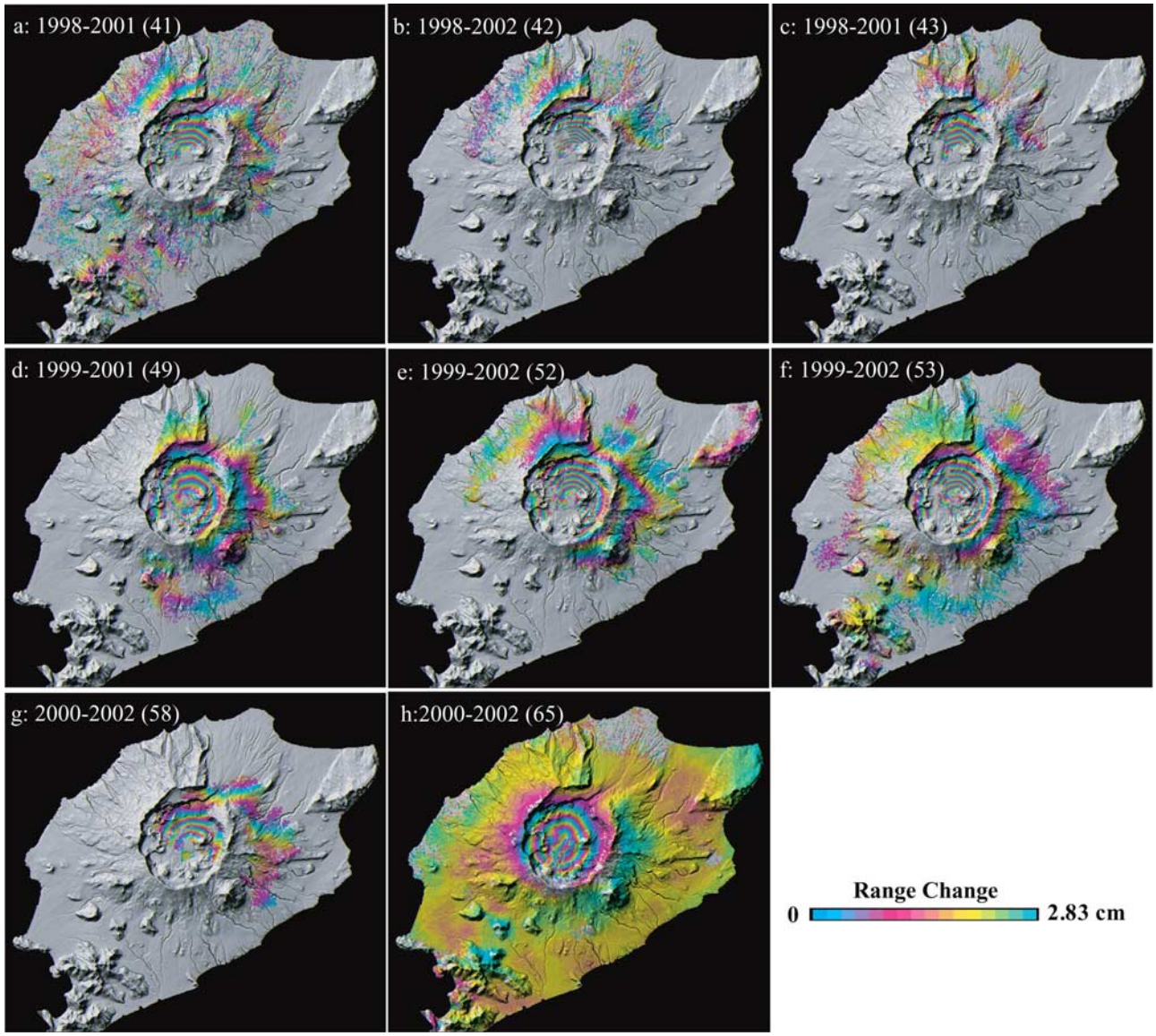

Figure 5. Examples of interferograms showing reinflation of Okmok volcano after its 1997 eruption. Each of these interferograms spans a time interval of multiple years. Each fringe (full color cycle) represents 2.83 cm of range change between the ground and the satellite. Additional information on SAR images used to produce the interferograms is given in Table 1. Areas that lack interferometric coherence are uncolored.

modeled successfully due to atmospheric contaminations or other unknown reasons, and were rejected from further investigation. There are more than 10^6 coherent pixels in each of the interferograms. To facilitate inverse modeling of the 59 interferograms that fit the 1-year or more interval criterion, we reduced the quantity of data in each interferogram using a quadtree algorithm [e.g., *Khawne et al.*, 2000; *Jonsson et al.*, 2002] following the protocol of *Masterlark and Lu* [2004]. This process reduces the number of data by about 2 orders of magnitude, depending on the characteristics of an individual interferogram.

[29] For each of the interferograms, we determined best fitting parameters for the location and strength of a dominant deformation source. We introduced linear terms in our models to account for a ramping phase due to uncertainties in satellite positions [*Massonnet and Feigl*, 1998]. To account for topographic departures from the half-space assumption, we adopted a simple method proposed by *Williams and Wadge* [1998] in which the depth of the source is adjusted according to the elevation of each computation point. There are seven unknowns for each model (x_1', x_2', x_3', ΔV, and three ramping-phase parameters). Following *Lu et al.* [2003b], we used the downhill simplex method and Monte Carlo simulations [*Press et al.*, 1992] to estimate optimal parameters and uncertainties. The root-mean-square error (RMSE) between the observed and modeled interferograms was used as the prediction fit criterion.

[30] We first investigated the spatial stability of the source during the 11-year study period by modeling each of the interferograms individually. The horizontal locations of the best fitting sources are shown in Figure 7. The semiaxes of

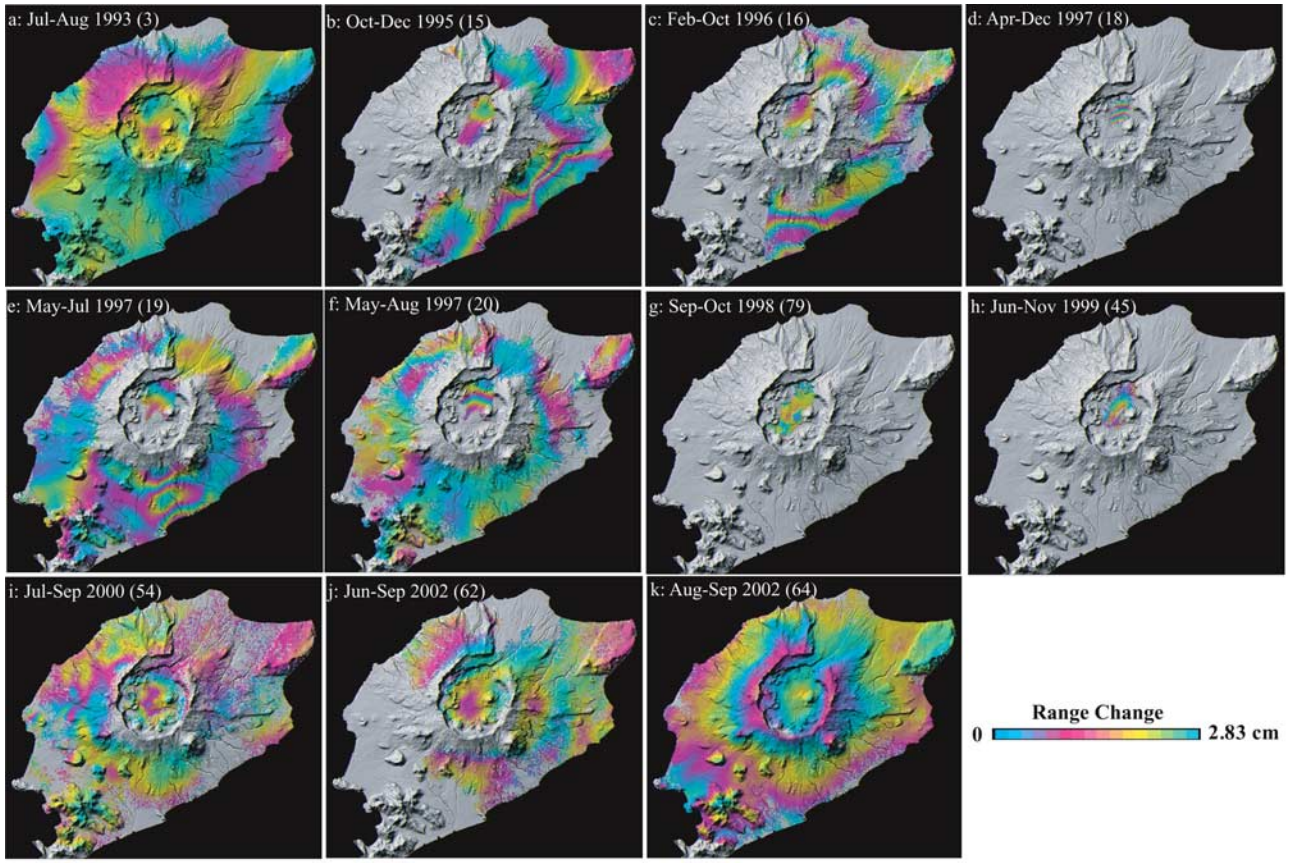

Figure 6. Examples of interferograms, each of which spans a time interval of less than 1 year. Each fringe (full color cycle) represents 2.83 cm of range change between the ground and the satellite. Additional information on SAR images used to produce the interferograms is given in Table 1. Areas that lack interferometric coherence are uncolored.

the ellipsoids represent the horizontal uncertainties of locations at one standard deviation (1σ). The modeled source locations are clustered at the center of the caldera and did not migrate significantly with time (Figure 7). On that basis, we assumed that the source for the preeruptive, coeruptive, and posteruptive deformation did not move laterally from 1992 to 2003.

[31] We then fixed the horizontal position of the deformation source using the weighted average of locations from the modeled interferograms and reestimated the remaining parameters. The resulting best fitting source depths, volume changes, and their uncertainties are shown in Figure 8. The error bars and circles represent the uncertainty bounds for depth and volume change at 1σ, respectively. The source depth for the preeruption and posteruption interferograms did not change appreciably from 1992 to 2003; the average source depth was 3.2 ± 0.2 km below sea level (about 3.6 km beneath the caldera floor). The depth for two 1995–1997 coeruption interferograms (Figures 2e and 2f) is slightly less than the average, but the difference (<400 m) is not significant at the 95% confidence level. In summary, the three-dimensional position of the source for preeruptive inflation, coeruptive deflation, and posteruptive inflation did not change significantly during the 11-year period of study.

[32] Because the estimated source locations were statistically identical and because the depth-strength ambiguity in (1) is inherent in inversions of a single component of three-

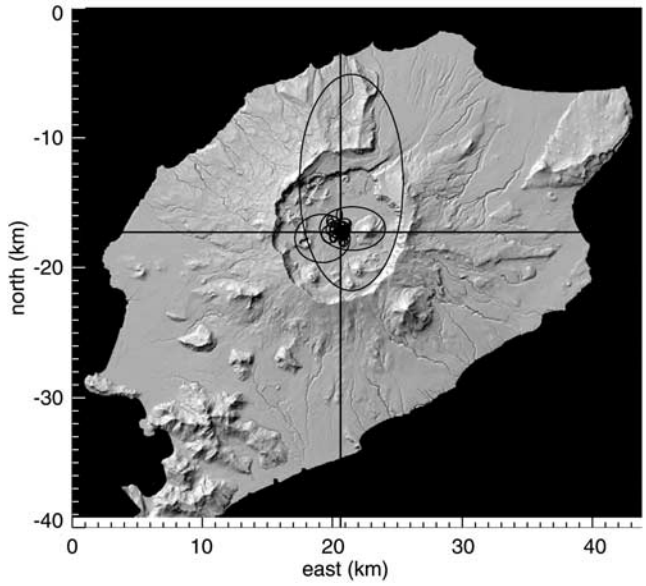

Figure 7. Estimated source positions superimposed on a shaded relief image of Okmok volcano. Uncertainty ellipses are plotted at 1σ. The cross indicates the weighted average horizontal position of the deformation source, which is centered on the caldera.

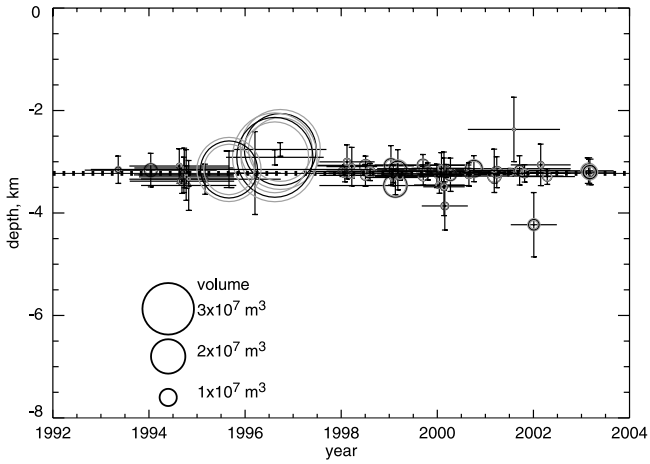

Figure 8. Estimated volume change and depth of the magma reservoir using the average horizontal position of modeled sources from Figure 7. Error bars and gray bounding circles represent 1σ uncertainties for depth and volume change (black circles) of the source, respectively. Horizontal bars denote the time span for each interferogram. The weighted average depth (dotted line) is about 3.2 km below sea level. Estimated volume changes for different interferograms using the fixed average location and depth of the magma reservoir are shown in Table 1.

dimensional deformation data [*Dieterich and Decker*, 1975], we reestimated the volume changes using a constant, average source location. Note that the relationship in (1) is linearized for the source volume if the position of the source is fixed. Thus we determined a least squares source-volume-change estimate for each modeled interferogram (Table 1).

[33] Inspired by the least squares approach that was used to retrieve the temporal deformation history from a sets of interferograms overlapping in time [*Berardino et al.*, 2002; *Usai*, 2003; *Schmidt and Burgmann*, 2003], we estimated the temporal evolution of the magma supply rate during 1992–2003 using the volume changes derived from 59 interferograms. The least squares approach acts to reduce the effects of atmospheric artifacts, which usually are associated with particular epochs and are not spatially correlated through time. Because all of the modeled interferograms are from SAR images acquired in the summer or fall, we could not resolve volume changes for time spans of less than 1 year. Therefore we only estimated volume change per year from 1992 to 2003 and scaled the volume changes for the 59 interferograms accordingly. For example, the volume change for a 2.2-year interferogram was scaled to that of 2-year interferogram by a factor of 0.909 (2/2.2), and the volume change for a 2.9-year interferogram was scaled to that of 3-year by a factor of 1.034 (3/2.9). Because the interferograms collectively span an 11-year interval, there are 11 mean, annual volume changes to be estimated. Since no interferogram starts or ends in 1994, we could only estimate the mean volume change for the period of 1993–1995. Therefore the total number of variables remaining to be determined is 10.

[34] If we define $\mathbf{\Delta V} = (\Delta V_1, \Delta V_2, \ldots, \Delta V_i, \ldots, \Delta V_m)$, where ΔV_i is the volume change for the ith of a total m interferograms, then the volume change per year, $\mathbf{q} = (q_1, q_2, \ldots, q_i, \ldots, q_n)$, is related to $\mathbf{\Delta V}$ by $\mathbf{\Delta V} = \mathbf{Gq}$, where $\mathbf{G}$ is a m by n (i.e., 59 by 10) binary matrix. Unity and null elements in each row correspond to the annualized temporal coverage for an interferogram. For example, if the ith interferogram spans a 3-year interval, the ith row of matrix $\mathbf{G}$ would have 3 consecutive 1 s in columns corresponding to the duration of the interferogram coverage.

[35] A weighting matrix, $\mathbf{w}$, was assembled by using the estimated volume change uncertainties for the diagonal elements. This assumes that the volume change estimates for the set of interferograms are uncorrelated. We pursued neither the validity nor the implications of this assumption. The weighted least squares solution [e.g., *Menke*, 1989] for $\mathbf{q}$ is

$$\mathbf{q} = \left[G^T \mathbf{w}^{-1} G\right]^{-1} G^T \mathbf{w}^{-1} \Delta V \tag{2}$$

Using (2), we estimated the annual volume change of the shallow reservoir beneath Okmok volcano, which we assume to be the magma influx per year, as a function of time (Figure 9). The variances of the estimated annual volume changes are the diagonal components of the inverse of the bracketed terms in (2). Before the 1997 eruption, the magma accumulation rate decreased from 6.4×10^6 m^3 yr^{-1} during 1992–1993, to 1.1×10^6 m^3 yr^{-1} during 1993–1995, and to -0.8×10^6 m^3 yr^{-1} during 1995–1996. The volume change associated with deflation of the volcano during the 1997 eruption is about $4.7 \pm 0.5 \times 10^7$ m^3. After the eruption, the magma accumulation rate was 4.1×10^6 m^3 yr^{-1} during 1997–1998, and it decreased to 0.8×10^6 m^3 yr^{-1} during 2000–2001. The rate increased again during 2001–2002 to a value similar to that for 1997–1998, but both of those rates are less than that during 1992–1993. The magma influx rate during 2002–2003 is similar to, and possibly greater than, the 1992–1993 rate. The rates for

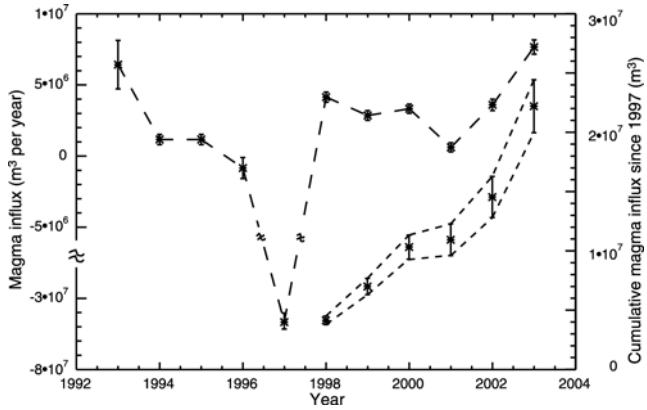

Figure 9. Estimated magma supply for the shallow reservoir as a function of time from 1992 to 2003. Incremental magma flux estimates (connected with dashed line) reveal annual supply dynamics. The vertical axis on the left applies to this curve. Error bars are 1σ. Cumulative magma storage following the 1997 eruption (with 1σ bounds) is shown in the lower right portion of the plot. The vertical axis on the right applies to the cumulative curve, which suggests that 30–60% of the volume erupted in 1997 (based on coeruption interferograms) has been replenished.

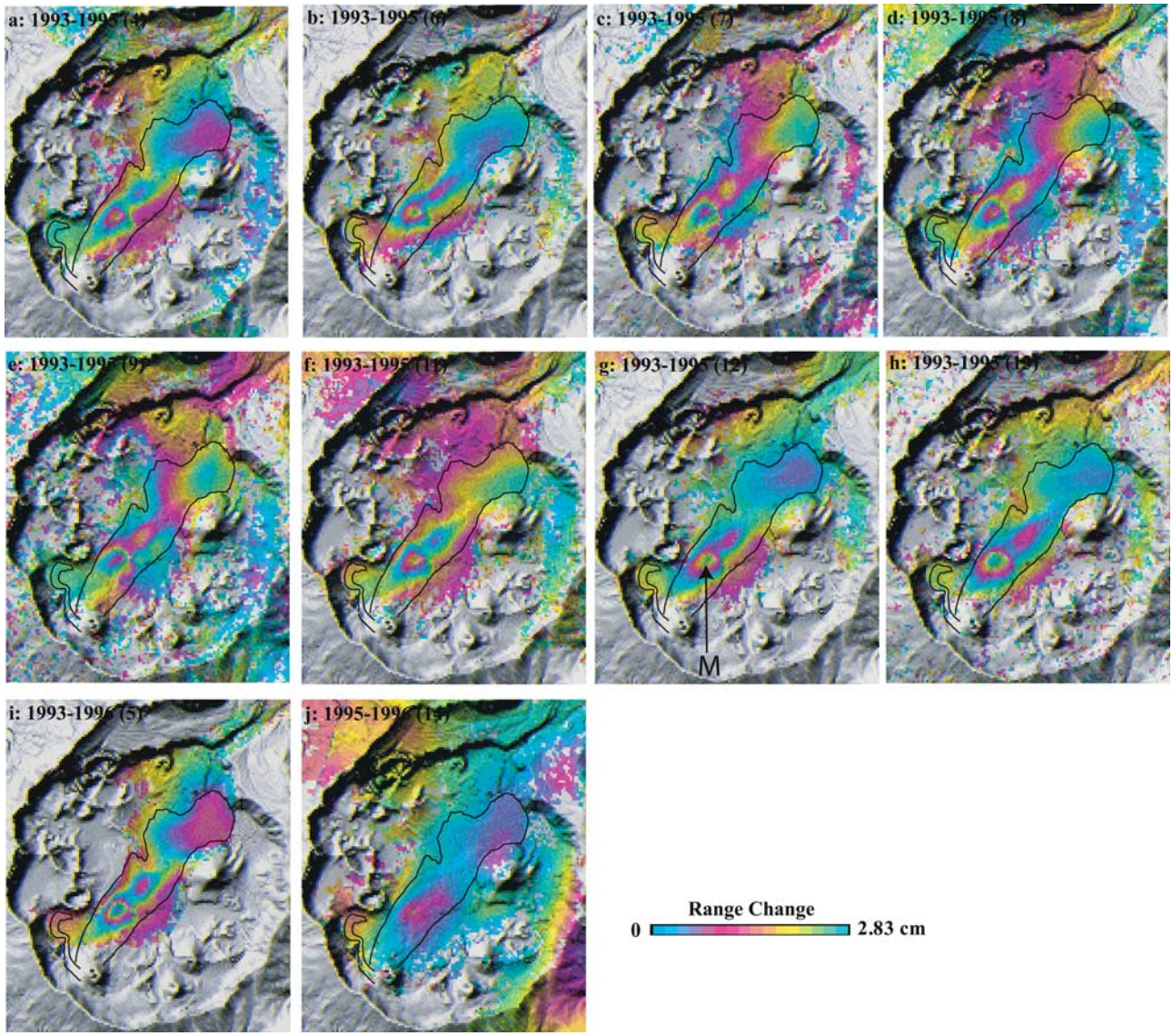

Figure 10. Observed postemplacement surface movement of 1958 lava flows after removing volcano-wide deformation based on the best fit model. One fringe (a full color cycle) represents 2.83 cm of range change along the satellite's look direction. The approximate extent of 1958 lava flows is outlined (see also Figure 1b). The time interval and identification number of each interferogram are labeled (see also Table 1). Areas that lack interferometric coherence are uncolored. The "M" in Figure 10g represents the location of maximum subsidence related to surface movement of the 1958 flows.

1992–1993 and 2002–2003 ($6 \sim 8 \times 10^6$ m^3 yr^{-1}) are the highest observed during the 11-year period of our study.

4. Analyses of Postemplacement Lava Flow Deformation

[36] For each of the 59 interferograms that were used to study volcanic deformation related to magma injection and extrusion, we obtained residual interferograms by removing the modeled deformation due to the spherical source with the fixed, average location. Inspection of the residual interferograms shows the source model fits the volcano-wide deformation quite well, as evidenced by small RMSE values ranging from a few mm to about 1 cm (Table 1). We examined several residual fringes that appear in two or more independent interferograms and determined that they are correlated both temporally and spatially (Figures 10 and 11). Therefore they are unlikely to be caused by atmospheric delay anomalies. Because the interferograms have different baselines and the DEM used to produce the deformation interferograms is accurate to less than 10 m, the residual fringes cannot have been caused by errors in the DEM. We concluded that they indicate local subsidence of the caldera floor both before and after the 1997 eruption.

[37] During 1993–1996, the residual fringes are associated with the 1958 lava flows, which trend approximately N45°W across the caldera floor (Figures 1b and 10). The maximum subsidence (M in Figure 10g) is located near the center of a line between Cone A, the vent for historical eruptions, and the center of the caldera. The mean subsidence rate was about 1.5 cm yr^{-1}. The relatively tight spatial extent of the deformation suggests a shallow source.

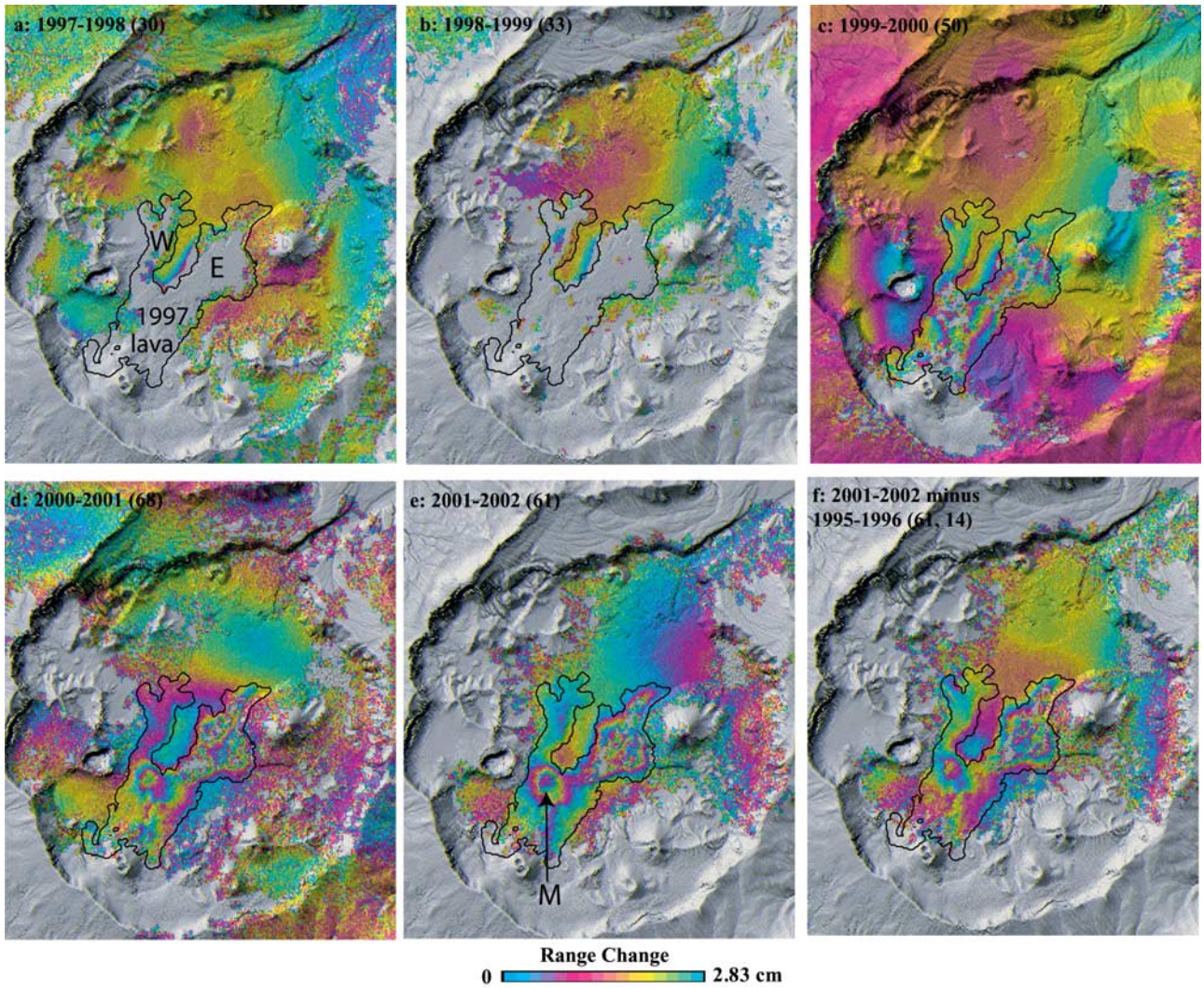

Figure 11. Observed postemplacement surface movement of 1958 and 1997 lava flows after removing volcano-wide deformation using a best fit model. One fringe (a full color cycle) represents 2.83 cm deformation along the satellite's look direction. The extent of 1997 lava flows is outlined (see also Figure 1b). The time interval and identification number of each interferogram are labeled (see also Table 1). Areas that lack interferometric coherence are uncolored. The "M" in Figure 11e represents the location of maximum subsidence related to surface movement of the 1958 lava flows (Figure 10g). The "W" and "E" represent the western and eastern lobes of the 1997 lava flows, respectively.

There is no fumarolic activity within the caldera like that associated with localized subsidence at other Aleutian volcanoes [*Lu et al.*, 2000b, 2002], so the intracaldera subsidence at Okmok is probably not due to hydrothermal activity. We do not have a DEM that represents the topography of Okmok before 1945, but we do have access to a hardcopy map in the U.S. Army Map Series that was produced for Okmok in 1943 (M. Shaffer, personal communication, 2003). The poor quality of the paper map made its conversion into a DEM difficult. However, we picked height values at a dozen locations on and near the 1958 lava flows from a digitized version of the map and compared them with corresponding heights from the pre-1997 DEM. Thus we determined that the average thickness of the 1945 and 1958 lava flows is about 25 m, which is consistent with the field report from BVE (1984). The thickest portions of the flows correspond to the areas of greatest subsidence suggested by the residual interferograms, so the subsidence is probably related to deformation of the 1945 and 1958 lava flows.

[38] Five post-1997 eruption residual interferograms, each of 1-year duration, are shown in Figure 11. Persistent subsidence of and near the 1997 lava flows is apparent in each of the images. Inspection led to the following observations:

[39] 1) Most of the 1997 lava flows are not coherent in 1997–1998 and 1998–1999 interferograms (Figures 11a and 11b). This suggests that the flow surfaces were changing enough to destroy coherence during the first two years after their emplacement, presumably as a result of thermal contraction and mechanical movement of unstable blocks. The 1997 flows retained partial coherence in the 1999–2000 interferograms (Figure 11c), and by 2000 most of the 1997 flow surface was coherent. During the entire time,

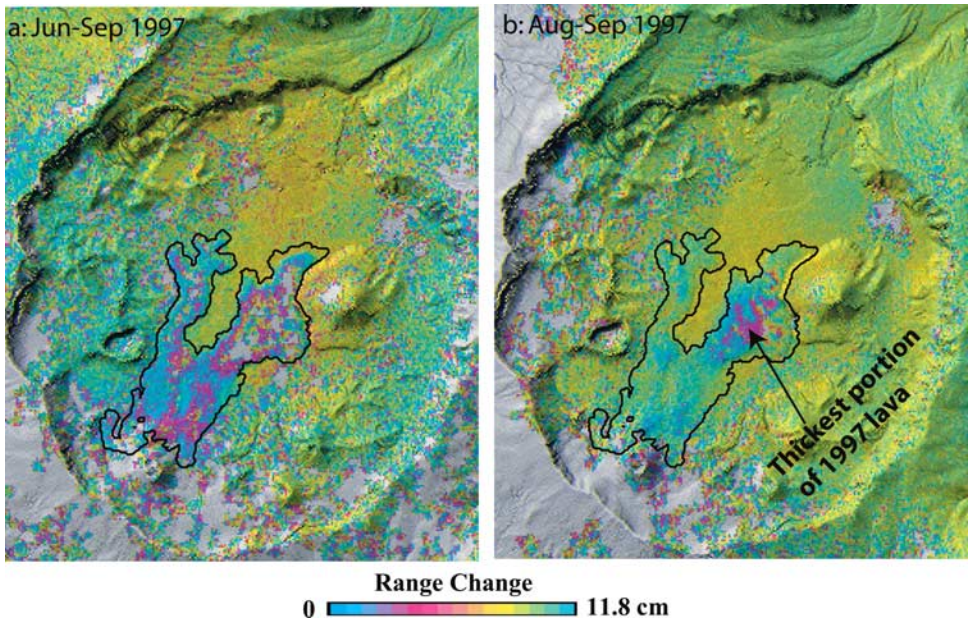

Figure 12. JERS-1 interferograms showing postemplacement surface movement of 1997 lava flows a few months after the 1997 eruption. One fringe (a full color cycle) represents 11.8 cm of range change along the satellite's look direction. The extent of 1997 lava flows is outlined (see also Figure 1b). The time interval and identification number of each interferogram are labeled (see also Table 1). Areas that lack interferometric coherence are uncolored. The thickest portion of the 1997 lava flows is marked.

coherence of the western lobe of the flows was higher than that of the thicker eastern lobe [*Lu et al.*, 2003a; *Patrick et al.*, 2003]. C band interferograms (Figure 6) that span less than a few months after the 1997 eruption were not coherent until the fall of 1998 (Figure 6h), so they are not useful for estimating the amount of subsidence that occurred in the months following the eruption. However, two JERS-1 interferograms for this period (Figure 12 and Table 1) have good coherence and show that parts of the 1997 flow subsided significantly. Maximum subsidence occurred on the thickest parts of the flows in the eastern lobe: more than 10 cm in 44 days during August–September 1997.

[40] 2) Deformation related to the 1997 flows extends into the 1958 flows. This is particularly clear on the 1958 flows between the western and eastern lobes of the 1997 flows. The sense of motion is such that parts of the 1958 flows adjacent to the 1997 flows subsided with respect to other parts of the 1958 flows (Figure 11). Subsidence of old lava flows due to loading by newly emplaced lava has been inferred from InSAR data for other volcanoes [*Briole et al.*, 1997; *Stevens et al.*, 2001], and we prefer that interpretation for this case as well.

[41] 3) In posteruption interferograms (Figures 11d–11f), systematic subsidence can be seen in the area (marked by M) where maximum subsidence was observed in the pre-1997 residual interferograms (Figure 10). This area was covered by a'a' flows in 1997 and was not coherent in 1-year interferograms in C band until 3 years later. At that time, the area was subsiding about 4 cm yr^{-1}. The 1997 flows are about 20 m thick in this area, which is similar to the average thickness of the flows in the western lobe (Figure 11) [*Lu et al.*, 2003a]. Therefore subsidence due to thermal contraction and compaction should be similar in these areas: 0.5∼1.0 cm during 2001–2002 (Figures 11e and 11f). After subtracting this amount of subsidence to account for compaction of the 1997 flows, we found that the area where maximum subsidence of 1.5 cm yr^{-1} was observed before the 1997 eruption continued to subside at a rate of 3.0∼3.5 cm yr^{-1} during 2001–2002. To illustrate this, we subtracted the 1995–1996 residual interferogram (Figure 10j) from the 2001–2002 residual interferogram (Figure 11e); the result is shown in Figure 11f. After the 1997 eruption, the subsidence rate of pre-1997 lava flows is about twice as great as that before the 1997 eruption.

[42] We attribute localized deformation within the caldera to the presence of young lava flows, primarily those emplaced in 1958 and 1997. Because the three-dimensional shape of the 1997 flows was known from comparison of preeruption and posteruption DEMs [*Lu et al.*, 2003a], we focused on deformation of the 1997 flows as revealed by the 1997–2002 interferograms (Figure 11). The results may also be pertinent to postemplacement deformation of the 1958 flows. We considered three possible deformation mechanisms: (1) poroelastic deformation of the caldera floor caused by the lava flow gravity load, (2) thermoelastic deformation of the lava flow due to cooling following emplacement, and (3) viscoelastic relaxation of the caldera floor caused by the lava flow gravity load [*Briole et al.*, 1997; *Stevens et al.*, 2001]. A rigorous quantitative analysis of the relative importance of these mechanisms would require numerical methods to account for complex three-dimensional geometries and heterogeneous distributions of subsurface material properties. Both the relatively low signal-to-noise ratio of the residual caldera deformation and the lack of subsurface structure constraints preclude such an analysis. Instead, we assumed a simplified geometry and conducted a qualitative analysis using two-dimensional finite element models (FEMs) of the

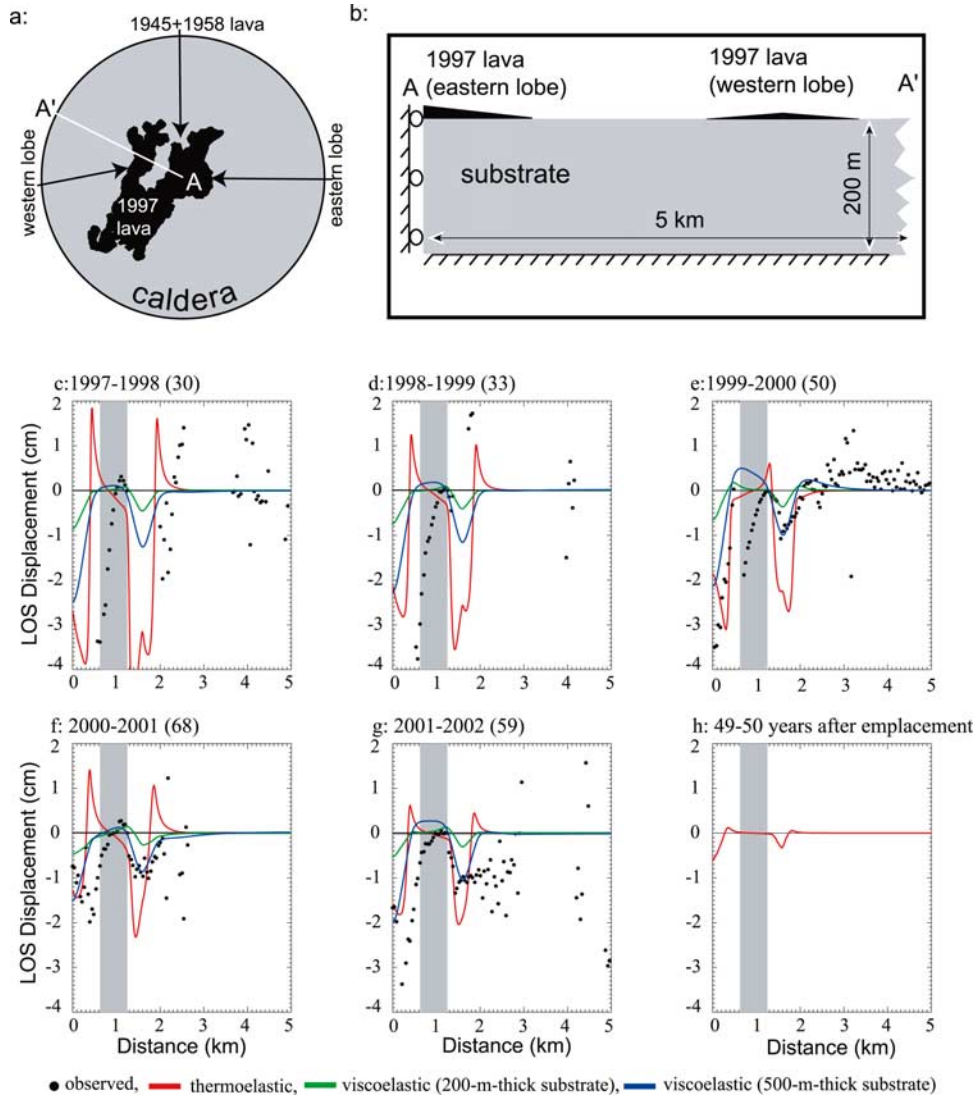

Figure 13. Postemplacement deformation models. (a and b) Two-dimensional FEM configuration used to study poroelastic, thermoelastic, and viscoelastic deformations due to the emplacement of 1997 lava flows. The model (Figure 13b) simulates plane strain conditions along a cross section A–A′ (Figure 13a). The vertical boundary at A is an axis of symmetry. The base and the vertical boundary at A′ are zero displacement. Additional configuration information is discussed in the text and material properties are summarized in Table 3. (c–g) Thermoelastic and viscoelastic deformation in several 1-year interferograms following the emplacement of 1997 lava flows.

caldera deformation for each of the three deformational mechanisms.

[43] The FEMs were constructed with the commercially available finite element code ABAQUS version 6.4 (HKS Inc., 2003, available at http://www.hks.com). This code allows for heterogeneous distributions of material properties and solves the governing equations for linear poroelastic [*Wang*, 2000], thermoelastic [*Biot*, 1956], and viscoelastic [*Jaeger*, 1969] behavior. The simulated plane strain problem domain includes a 200-m-thick caldera substrate (Figures 13a–13b). The southeast edge is a symmetry boundary at the center of the caldera. The problem domain extends 5 km laterally to the northwest from the center to the edge of the caldera. The northwest edge and bottom of the substrate are fixed. The tops of the lava flow sections are free surfaces. The top portions of the substrate not covered by lava are free surfaces. The thickness of lava in the eastern lobe decreases linearly from 50 m at the symmetry boundary to zero at the margin of the lobe. The thickness of lava in the western lobe is 25 m at the center of the section and decreases linearly on both sides to zero at the margins. Details of the four FEM configurations are illustrated in Figure 13, and material properties are from *Stevens et al.* [2001] and *Turcotte and Schubert* [1982] and are summarized in Table 3.

[44] We first explored the possibility that the localized deformation in Figure 11 was poroelastic deformation caused by the lava flow gravity load. In this configuration, the substrate represents a 200-m-thick layer of a compliant material having a significant saturated porosity. Transient poroelastic deformation is caused by the decay of excess pore fluid pressures initiated by the gravity load of the

Table 3. Material Properties Used for Caldera Deformation Models

	Poroelastic	Thermoelastic	Viscoelastic
Young's modulus, Pa	2.5×10^9	2.5×10^9	2.5×10^9
Poisson's ratio	0.25	0.25	0.25
Density,[a] kg m^{-3}	2000	2000	2000
Unjacketed compressibility	2.9×10^{10}		
Pore fluid compressibility	3.3×10^9		
Thermoelastic expansion coefficient, K^{-1}		10^{-5}	
Specific heat, J kg^{-1} °K^{-1}		1250	
Viscosity, Pa s			10^{17}

[a]Basalt and 33% porosity.

newly emplaced lava. The initial response of the poroelastic substrate to this loading is undrained, because the load propagates much faster than the pore fluids in the substrate can flow in response to the distribution of excess pore fluid pressure. For undrained conditions, the substrate is relatively stiff (with respect to the drained conditions), because the pore fluids bear a portion of the load as excess pore fluid pressure [*Wang*, 2000]. Over time and with constant loading, the portion of the load borne by the pore fluids is transferred to the substrate matrix as the pore fluids flow in response to the excess pore fluid pressure distribution. As the excess pore fluid pressure decays, the substrate conditions migrate from undrained (stiff) to drained (compliant) conditions. This gradual change from stiff to compliant substrate behavior is the essence of transient poroelastic deformation. In our case, the magnitude of the predicted poroelastic deformation can reach more than 5 cm. However, the bulk of the response for this relatively local flow system occurs within the few days following the loading event for hydraulic conductivities as low as 10^{-12} m s^{-1}. Over the 1-year time span of the 1997–1998 interferogram (Figure 11a), which begins several months after the 1997 eruption, the poroelastic deformation is negligible. Therefore poroelastic response due to emplacement of the 1997 lava flows cannot account for the temporal persistence of deformation shown in Figure 11.

[45] We next explored thermoelastic deformation of the 1958 and 1997 flows due to cooling after emplacement. The initially hot lava is emplaced on top of the relatively cool substrate. The assumed initial conditions for this system are T_0 = 1000°C and 0°C for the lava and substrate, respectively. Temperature gradients set up by the initial conditions drive transient heat flow from the hot flows into the substrate. Both lava flows contract as heat is lost into the substrate. We considered two configurations for the substrate. First, we assumed the substrate was an adiabatic system with the same material properties as the lava flows. In this case, the lava contracts from heat loss but the substrate expands from the influx of heat. Results from this configuration predict a sustained transient deformation, but the spatial characteristics poorly simulate the observed deformation. Therefore we rejected this model. Next, we assumed the substrate is an elastic heat sink such that groundwater efficiently transports heat away from the lava flows and out of the system. In this case, the substrate serves as a highly conductive elastic medium welded to the base of the lava flows. Predictions from this model reasonably approximate the spatial and temporal characteristics of the observed deformation for some of the posteruption interferograms (Figures 13b–13f). Therefore this second configuration is our preferred thermoelastic model. The actual system is most likely better described as having a substrate somewhere in between the two end-members considered. Unfortunately, we lack the constraining data required to resolve this issue.

[46] Finally, we examined the viscoelastic relaxation of the caldera floor (i.e., 1958 lava) caused by the lava flow gravity load (i.e., 1997 lava). Transient viscoelastic deformation is caused by viscous flow in response to the deviatoric stresses in the substrate initiated by the lava emplacement. This model is very similar to the poroelastic model, with the exception of the substrate treatment. Instead of a poroelastic substrate, the substrate was assumed to be a linear viscoelastic material [*Briole et al.*, 1997; *Stevens et al.*, 2001]. The gravity load of the newly emplaced lava is initially in static equilibrium and behaves as a simple elastic material. With time, the substrate flows in response to the deviatoric stresses initiated by the loading. The rate of viscous flow is controlled by a viscosity parameter. For the assumed 200-m thickness, the predicted deformation is persistent through time, although the magnitude of the deformation is insufficient to account for the observed residual deformation. Increasing the substrate thickness (Figure 13) or the viscosity increases the magnitude of the predicted viscoelastic deformation. The observed deformation on and near the 1997 flows is most likely due in part to the viscoelastic response of the caldera floor to loading by the 1997 lava flows.

[47] Because these two-dimensional FEMs have rather simplified geometries and material properties, they do not fit the observations very well. However, our analysis provides clues toward identifying the dominant mechanisms that caused the observed deformation. We believe the persistent deformation in Figure 11 was most likely caused by a combination of thermoelastic deformation of the lava flows due to cooling following emplacement and viscoelastic responses to the gravity loads of the newly emplaced lava flows.

[48] What is the likely mechanism for the subsidence of pre-1997 lava flows observed in the 1993–1996 interferograms (Figure 10)? To answer this question, we calculated the theoretical subsidence rate from thermoelastic contraction of the 1997 flows 50 years after their emplacement. The result is about 7 mm yr^{-1} (Figure 13h). The pre-1997 flows are a'a' from several historical eruptions, including 1945 and 1958. Each of these is probably comparable in thickness to the 1997 flow (20 $\sim$ 30 m), so each can be expected to contribute $\sim$7 mm yr^{-1} to present-day subsidence, even 50 years after their emplacement. We concluded that the observed subsidence of about 1.5 cm yr^{-1} for pre-1997 flows, can be explained by thermoelastic contraction of the pre-1997 flows themselves.

5. Discussion and Conclusions

[49] Our analysis of interferograms for Okmok volcano that collectively span the 1992–2003 period, which includes the 1997 eruption, indicates that a magma reservoir beneath the center of the caldera and about 3 km below sea level was responsible for volcano-wide deformation before, during, and after the eruption. Magma filled this reservoir at

a rate that varied both before and after the eruption, causing volcano-wide inflation. We infer that, when the magma pressure within the reservoir reached a certain threshold, an eruption ensued. Withdrawal of magma depressurized the reservoir, causing volcano-wide deflation, and fed surface lava flows. Magma started to accumulate in the reservoir soon after the eruption stopped, initiating a new intereruption strain cycle.

[50] The inferred rate of magma filling during 1992–1996 decayed with time and became negative in the 1995–1996 period (Figure 9). A decaying pattern of inflation before eruptions has been observed for other shield volcanoes [*Dvorak and Dzurisin*, 1997], including Westdahl volcano, located about 200 km northeast of Okmok [*Lu et al.*, 2003b]. The diminishing pressure gradient between a shallow magma reservoir that is pressurizing and a deep source could account for a decreasing magma supply rate [*Dvorak and Okamura*, 1987; *Lu et al.*, 2003b]. The absence of inflation during 1995–1996 might indicate a critical state of pressurization for the reservoir, in which the surrounding country rock is strong enough to temporarily retard the magma supply from depth. For a frequently active basaltic volcano such as Okmok, a change from inflation to deflation during a noneruptive period might serve as a recognizable precursor to an eruption.

[51] It is instructive to compare the behavior of Okmok with the well-studied precursory behavior of the 1980 eruption of Mount St. Helens. Although the situation was considerably different at Mount St. Helens during the growth of a dacite lava dome from 1980 to 1986, a similar pattern of progressive inflation followed by sudden deflation was diagnostic of the onsets of several dome-growth episodes. In that case, the inflation rate typically increased dramatically during the final weeks to days before intruding magma broke onto the surface of the dome. This repetitive pattern, together with increasing shallow seismicity beneath the dome, was the basis for several successful predictions [*Swanson et al.*, 1983]. In most cases, the surface outbreak was marked within a matter of hours by a sharp reversal in the direction of ground tilt recorded by electronic tiltmeters on or near the dome - from radial outward (inflation) to radial inward (deflation) [*Dzurisin et al.*, 1983]. The runaway nature of preeruption inflation at Mount St. Helens during dome building, in contrast to slowing inflation at Okmok before its 1997 eruption, might reflect some combination of the magma supply rate as a function of time and the relative strength of the host rock. We infer that at Mount St. Helens the thermally weakened shallow conduit system and embryonic lava dome offered little resistance to upward magma flow in the first few years following the large 1980 landslide and eruption. As a result, once a batch of buoyant magma began its ascent toward the dome, the system as a whole yielded relatively easily and the process accelerated to completion. At Okmok, it seems, the rock hosting the shallow reservoir and the conduit system above it provided enough resistance to overcome the differential magma pressure and shut off the supply for a time during 1995–1996. Exsolution of magmatic volatiles during this period and resulting vesiculation might have triggered the eventual eruption. Experience at other volcanoes suggests that the most common pattern is a steady or increasing inflation rate as an eruption draws near. However, there might exist a complete spectrum between those cases and ones in which the inflation rate slows as a function of time before some other process tips the balance either toward or away from an eruption (e.g., vesiculation or cooling and crystallization, respectively). This possibility recommends caution in the interpretation of a declining inflation rate, especially if lives are at stake.

[52] The 1995–1997 coeruption interferograms suggest a volume decrease of the shallow reservoir of about 0.05 ± 0.01 km^3. The calculated bulk volume of the 1997 lava flows is 0.15 ± 0.03 km^3 [*Lu et al.*, 2003a], which is similar to the volume of the 1958 flows (0.12 km^3) (BVE, 1984). Before comparing these extruded volumes to the inferred volume changes in the reservoir, it was necessary to correct for void space in the flows created by vesiculation. The 1997 lava flow is similar to typical Hawaiian a'a' lava, with vesicularity ranging from 25% to 75% [*Cashman et al.*, 1994]. Therefore the estimated dense rock equivalent volume of the 1997 flows is 0.11 ± 0.04 km^3, and the inferred volume change for the reservoir is less by roughly a factor of two. The discrepancy could be caused by many factors such as oversimplication of the modeled source, and heterogeneity of caldera structure and material properties. For example, the source volume change derived from deformation data depends on the compressibility of magma in the reservoir [*Johnson et al.*, 2000], a factor that we ignored in our analysis. The presence of exsolved gas tends to increase the source volume change estimated from deformation data, so our calculation is likely to be an underestimate of the actual volume change in the reservoir. In addition, the ring faults bordering the caldera can change the ground surface deformation pattern. It has been demonstrated that inversion of ground surface deformation without considering boundary fractures marking the caldera collapse tends to locate a shallower magmatic source, and consequently less volume change than there actually is [*De Natale and Pingue*, 1993; *Beauducel et al.*, 2004]. Therefore the volume of the 1997 eruption derived from modeling coeruption interferograms with a simple Mogi source can underestimate the true volume.

[53] Our modeling indicates that the magma supply rate to the shallow reservoir is not constant, ranging from nearly 0 to 8 × 10^6 m^3 yr^{-1}, with an average of about 4 × 10^6 m^3 yr^{-1}. By the summer of 2003, the reservoir had been replenished with about 2.2 ± 0.2 × 10^7 m^3 of magma since the end of the 1997 eruption. Assuming there was no significant inflation between October 1996 and February 1997, the volume of newly accumulated magma is 30 ∼ 60% of that erupted in 1997 (0.05 ± 0.01 km^3 based on coeruption interferograms).

[54] In addition to volcano-wide deformation related to magma injection and extrusion, our interferograms reveal local deformation associated with young lava flows. For example, the 1993–1996 interferograms suggest that parts of the 1958 lava flows could be subsiding as much as 1.5 cm yr^{-1} (Figure 10). The subsidence is most likely caused by thermoelastic contraction from cooling of the 1958 flows, which are as much as 20∼30 m thick (BVE, 1984). The thickness distribution of the 1958 flows is not known, but the heterogeneous pattern of subsidence (Figure 10) strongly implies that it is not uniform. Neither

are the 1997 flows uniformly thick, as shown by differencing preeruption and posteruption DEMs.

[55] A second piece of evidence for postemplacement deformation of lava flows is that the 1997 flow surfaces were not coherent in C band interferograms with 1-year separation until 3 years after the eruption. This suggests significant surface movement associated with lava cooling and consolidation [*Stevens et al.*, 2001]. On the basis of L band JERS-1 interferograms (Figure 12), surface displacements due to lava contraction and consolidation can be 2 mm d^{-1} or more four months after emplacement. This is similar to the contraction rate of young lava flows observed at Mount Etna volcano, Italy [*Stevens et al.*, 2001; *Briole et al.*, 1997].

[56] A third example is local subsidence of pre-1997 flows, which we attribute to loading by 1997 flows. Two-dimensional FEM analysis suggests that the deformation is due to thermoelastic and viscoelastic response of the older flows and substrate to the overlying 1997 lava.

[57] In summary, there are several deformation fields in each of the coherent interferograms produced from SAR images acquired after the 1997 eruption: (1) volcano-wide inflation due to magma influx into the shallow reservoir; (2) thermoelastic subsidence of pre-1997 lava flows, some of which are covered by 1997 lava; (3) deformation of pre-1997 lava flows due to loading by 1997 lava; and (4) subsidence of 1997 lava flows due to thermal contraction and consolidation [*Stevens et al.*, 2001]. These deformation fields are superimposed and possibly coupled with each other to produce a complex deformation system. The local deformation of lava surfaces provides constraints on physical and rheological properties of the flows. On the other hand, local deformation tends to contaminate volcano-wide deformation caused by magma movements, which has implications for the siting of geodetic markers or instruments.

[58] With the advance of satellite InSAR, volcano geodesy has entered a new era [*Dzurisin*, 2003]. Deformation patterns have been revealed by InSAR at dozens of the world's volcanoes [e.g., *Amelung et al.*, 2000; *Lu et al.*, 2003c; *Massonnet et al.*, 1995; *Massonnet and Sigmundsson*, 2000; *Pritchard and Simons*, 2002; *Sigmundsson et al.*, 1999; *Wicks et al.*, 1998; *Zebker et al.*, 2000], including evidence for inflation before eruptions, deflation associated with lava extrusion, inflation due to dike opening prior to eruption, intermittent inflation associated with pulses of magma injection at volcanoes with long repose periods, and local deformation associated with young lava flows. This rich and growing collection of InSAR data, together with ground-based geodetic observations, seismic data, gravity measurements, and studies of volcanic gas emissions, is helping to illuminate the plumbing systems of active volcanoes. Combined with advanced statistics and modeling analysis, such information can be the basis for reliable eruption forecasts [*Sparks*, 2003].

[59] **Acknowledgments.** ERS-1 and ERS-2, RADARSAT-1, and JERS-1 SAR images are copyright 1991–2003 European Space Agency (ESA), Canadian Space Agency (CSA), and Japan Aerospace Exploration Agency (JAXA), respectively, and were provided by the Alaska Satellite Facility (ASF) and JAXA. This research was supported by funding from NASA (NRA-99-OES-10 RADARSAT-0025-0056), and in part by the USGS contract O3CRCN0001 and the USGS Land Remote Sensing Program and Volcano Hazards Program. We thank ASF and JAXA for the excellent support to provide SAR data on a timely basis; N. Stevens, an anonymous reviewer, and the Associate Editor for technical reviews; C. Wicks and B. Ramachandran for USGS internal review; C. Wicks for assistance on deformation modeling; T. Neal, C. Nye, D. Grey, and Ken Papp for many insightful discussions regarding Okmok lava flows and post-emplacement lava flow deformation; P. Briole and G. Wadge for insightful discussion on deformation mechanisms; D. Grey for kindly giving us a copy of her thesis; and M. Shaffer for providing a copy of U.S. Army Map Series.

References

Amelung, F., S. Jonsson, H. Zebker, and P. Segall (2000), Widespread uplift and "trapdoor" faulting on Galapagos volcanoes observed with radar interferometry, *Nature*, *407*, 993–996.

Beauducel, F., P. Briole, and J. L. Froger (2000), Volcano-wide fringes in ERS satellite radar interferograms of Etna (1992–1998), Deformation or tropospheric effect?, *J. Geophys. Res.*, *105*, 16,391–16,402.

Beauducel, F., G. De Natale, F. Obrizzo, and F. Pingue (2004), 3-D modeling of Campi Flegrei ground deformations: Role of caldera boundary discontinuities, *Pure Appl. Geophys.*, *161*, doi:10.1007/s00024-004-2507-4.

Berardino, P., G. Fornaro, R. Lanari, and E. Sansosti (2002), A new algorithm for surface deformation monitoring based on small baseline differential SAR interferograms, *IEEE Trans. Geosci. Remote Sens.*, *40*, 2375–2383.

Biot, M. A. (1956), Thermoelasticity, and irreversible thermodynamics, *J. Appl. Phys.*, *27*(3), 240–253.

Briole, P., D. Massonnet, and C. Delacourt (1997), Post-eruptive deformation associated with the 1986–87 and 1989 lava flows of Etna detected by radar interferometry, *Geophys. Res. Lett.*, *24*, 37–40.

Byers, F. M. (1959), Geology of Umnak and Bogoslof Islands, Aleutian Islands, Alaska, *U. S. Geol. Surv. Bull.*, *1028-L*, 167–369.

Byers, F. M., Jr., D. M. Hopkins, K. L. Wier, and B. Fisher (1947), Part 3: Volcano investigations on Umnak Island, 1946, *Alaskan Volcano Invest. Rep. 2, Progr. Invest. 1946*, pp. 19–53, U.S. Geol. Surv., Reston, Va.

Cashman, K. V., M. T. Mangan, and S. Newman (1994), Surface degassing and modifications to vesicle size distributions in active basalt flows, *J. Volcanol. Geotherm. Res.*, *61*, 45–68.

Dean, K., M. Servilla, A. Roach, B. Foster, and K. Engle (1998), Satellite monitoring of remote volcanoes improves study efforts in Alaska, *Eos Trans. AGU*, *79*(35), 413, 422–423.

De Natale, G., and F. Pingue (1993), Ground deformation in collapsed caldera structures, *J. Volcanol. Geotherm. Res.*, *57*, 19–38.

Dieterich, J. H., and R. W. Decker (1975), Finite element modeling of surface deformation associated with volcanism, *J. Geophys. Res.*, *80*, 4094–4102.

Dvorak, J., and D. Dzurisin (1997), Volcano geodesy: The search for magma reservoirs and the formation of eruptive vents, *Rev. Geophys.*, *35*, 343–384.

Dvorak, J., and A. T. Okamura (1987), A hydraulic model to explain variations in summit tilt rate at Kilauea and Mauna Loa volcanoes, in *Volcanism in Hawaii*, edited by R. W. Decker, T. L. Wright, and P. H. Stauffer, *U.S. Geol. Surv. Prof. Pap.*, *1350*, 1281–1296.

Dzurisin, D. (2003), A comprehensive approach to monitoring volcano deformation as a window on the eruption cycle, *Rev. Geophys.*, *41*(1), 1001, doi:10.1029/2001RG000107.

Dzurisin, D., J. A. Westphal, and D. J. Johnson (1983), Eruption prediction aided by electronic tiltmeter data at Mount St. Helens, *Science*, *221*, 1381–1383.

Gatelli, F., et al. (1994), The wavenumber shift in SAR interferometry, *IEEE Trans. Geosci. Remote Sens.*, *32*, 855–865.

Grey, D. (2003), Post-caldera eruptions at Okmok volcano, Umnak Island, Alaska, with emphasis on recent eruptions from Cone A., M.S. thesis, Univ. of Alaska, Fairbanks, Dec.

Jaeger, J. C. (1969), *Elasticity, Fracture and Fluid Flow*, 268 pp., Methuen, New York.

Johnson, D. J., F. Sigmundsson, and P. T. Delaney (2000), Comment on "Volume of magma accumulation or withdrawal estimated from surface uplift or subsidence, with application to the 1960 collapse of Kilauea volcano" by P. T. Delaney and D. F. McTigue, *Bull. Volcanol.*, *61*, 491–493.

Jonsson, S., H. Zebker, P. Segall, and F. Amelung (2002), Fault slip distribution of the 1999 *Mw* 7.1 Hector Mine earthquake, California, estimated from satellite radar and GPS measurements, *Bull. Seismol. Soc. Am.*, *92*, 1377–1389.

Khawne, A., S. Omsin, S. Noppanakeepong, and K. Wongrujira (2000), Subband SAR image coding by using quadtree decomposition on variable block truncation code, paper presented at Asian Conference on Remote Sensing, Asian Assoc. on Remote Sens., Taipei, Taiwan.

Lu, Z., and J. Freymueller (1998), Synthetic aperture radar interferometry coherence analysis over Katmai volcano group, Alaska, *J. Geophys. Res.*, *103*, 29,887–29,894.

Lu, Z., D. Mann, and J. Freymueller (1998), Satellite radar interferometry measures deformation at Okmok Volcano, *Eos Trans. AGU*, *79*(39), 461, 467–468.

Lu, Z., D. Mann, J. Freymueller, and D. Meyer (2000a), Synthetic aperture radar interferometry of Okmok volcano, Alaska: Radar observations, *J. Geophys. Res.*, *105*, 10,791–10,806.

Lu, Z., C. Wicks, J. Power, and D. Dzurisin (2000b), Ground deformation associated with the March 1996 earthquake swarm at Akutan volcano, Alaska, revealed by satellite radar interferometry, *J. Geophys. Res.*, *105*, 21,483–21,496.

Lu, Z., T. Masterlark, J. Power, D. Dzurisin, and C. Wicks (2002), Subsidence at Kiska volcano, western Aleutians, detected by satellite radar interferometry, *Geophys. Res. Lett.*, *29*(18), 1855, doi:10.1029/2002GL014948.

Lu, Z., E. Fielding, M. Patrick, and C. Trautwein (2003a), Estimating lava volume by precision combination of multiple baseline spaceborne and airborne interferometric synthetic aperture radar: The 1997 eruption of Okmok volcano, Alaska, *IEEE Trans. Geosci. Remote Sens.*, *41*, 1428–1436.

Lu, Z., T. Masterlark, D. Dzurisin, R. Rykhus, and C. Wicks (2003b), Magma supply dynamics at Westdahl Volcano, Alaska, modeled from satellite radar interferometry, *J. Geophys. Res.*, *108*(B7), 2354, dio:10.1029/2002JB002311.

Lu, Z., C. Wicks, D. Dzurisin, J. Power, W. Thatcher, and T. Masterlark (2003c), Interferometric synthetic aperture radar studies of Alaska volcanoes, *Earth Obs. Mag.*, *12*(3), 8–18.

Lu, Z., C. Wicks, O. Kwoun, J. Power, and D. Dzurisin (2005), Surface deformation associated with the March 1996 earthquake swarm at Akutan Island, Alaska, revealed by C-band ERS and L-band JERS radar interferometry, *Can. J. Remote Sens.*, in press.

Madsen, S., J. Martin, and H. Zebker (1995), Analysis and evaluation of the NASA/JPL TOPSAR across-track interferometric SAR system, *IEEE Trans. Geosci. Remote Sens.*, *33*, 383–391.

Mann, D., J. Freymueller, and Z. Lu (2002), Deformation associated with the 1997 eruption of Okmok volcano, Alaska, *J. Geophys. Res.*, *107*(B4), 2072, doi:10.1029/2001JB000163.

Massmann, F. H. (1995), Information for ERS PRL/PRC users, technical note, GeoForschungsZentrum Potsdam, Potsdam, Germany.

Massonnet, D., and K. Feigl (1998), Radar interferometry and its application to changes in the Earth's surface, *Rev. Geophys.*, *36*, 441–500.

Massonnet, D., and F. Sigmundsson (2000), Remote sensing of volcanic deformation by radar interferometry from various satellites, in *Remote Sensing of Active Volcanism*, *Geophys. Monogr. Ser.*, vol. 116, edited by P. Mouginis-Mark et al., pp. 207–221, AGU, Washington, D. C.

Massonnet, D., P. Briole, and A. Arnaud (1995), Deflation of Mount Etna monitored by spaceborne radar interferometry, *Nature*, *375*, 567–570.

Masterlark, T., and Z. Lu (2004), Transient volcano deformation sources imaged with InSAR: Application to Seguam island, *J. Geophys. Res.*, *109*, B01401, doi:10.1029/2003JB002568.

McCann, G. D., and C. H. Wilts (1951), A mathematical analysis of the subsidence in the Long Beach-San Pedro area, report, Calif. Inst. of Technol., Pasadena.

McGimsey, R. G., and K. L. Wallace (1999), 1997 volcanic activity in Alaska and Kamchatka: Summary of events and response of the Alaska Volcano Observatory, *U.S. Geol. Surv. Open File Rep., 99-448*, 18–23.

Menke, W. (1989), *Geophysical Data Analysis: Discrete Inverse Theory*, *Int. Geophys. Ser.*, vol. 45, 289 pp., Springer, New York.

Miller, T. P., et al. (1998), Catalog of the historically active volcanoes of Alaska, *U.S. Geol. Surv. Open File Rep., 98-582*, 104 pp.

Mogi, K. (1958), Relations between the eruptions of various volcanoes and the deformations of the ground surface around them, *Bull. Earthquake Res. Inst. Univ. Tokyo*, *36*, 99–134.

Murakami, M., M. Tobita, S. Fujiwara, T. Saito, and H. Massaharu (1996), Coseismic crustal deformations of 1994 Northridge California earthquake detected by interferometric JERS-1 SAR, *J. Geophys. Res.*, *101*, 8605–8614.

Patrick, M. R., J. Dehn, K. R. Papp, Z. Lu, L. Moxey, K. G. Dean, and R. Guritz (2003), The 1997 eruption of Okmok Volcano, Alaska: A synthesis of remotely sensed imagery, *J. Volcanol. Geotherm. Res.*, *127*, 89–107.

Pritchard, M., and M. Simons (2002), A satellite geodetic survey of large-scale deformation of volcanic centers in the central Andes, *Nature*, *418*, 167–171.

Press, W., S. Teukolsky, W. Vetterling, and B. Flannery (1992), *Numerical Recipes in C: The Art of Scientific Computing*, 994 pp., Cambridge Univ. Press, New York.

Rosen, P., S. Hensley, H. Zebker, F. H. Webb, and E. J. Fielding (1996), Surface deformation and coherence measurements of Kilauea volcano, Hawaii, from SIR-C radar interferometry, *J. Geophys. Res.*, *101*, 23,109–23,125.

Rosen, P. A., et al. (2000), Synthetic aperture radar interferometry, *Proc. IEEE*, *88*, 333–380.

Scharroo, R., and P. Visser (1998), Precise orbit determination and gravity filed improvement for the ERS satellites, *J. Geophys. Res.*, *103*, 8113–8127.

Schmidt, D., and R. Burgmann (2003), Time-dependent land uplift and subsidence in the Santa Clara valley, California, from a large interferometric synthetic aperture radar data set, *J. Geophys. Res.*, *108*(B9), 2416, doi:10.1029/2002JB002267.

Sigmundsson, F., P. Durand, and D. Massonnet (1999), Opening of an eruptive fissure and seaward displacement at Piton de la Fournaise volcano measured by RADARSAT satellite radar interferometry, *Geophys. Res. Lett.*, *26*, 533–536.

Sparks, R. S. J. (2003), Forecasting volcanic eruptions, *Earth Planet. Sci. Lett.*, *210*, 1–15.

Stevens, N. F., G. Wadge, C. A. Williams, J. G. Morley, J. P. Muller, J. B. Murray, and M. Upton (2001), Surface movements of emplaced lava flows measured by synthetic aperture radar interferometry, *J. Geophys. Res.*, *106*, 11,293–11,313.

Swanson, D. A., T. J. Casadevall, D. Dzurisin, S. D. Malone, C. G. Newhall, and C. S. Weaver (1983), Predicting eruptions at Mount St. Helens, June 1980 through December 1982, *Science*, *221*, 1369–1376.

Turcotte, D., and G. Schubert (1982), *Geodynamics: Applications of Continuum Physics to Geological Problems*, 450 pp., John Wiley, New York.

Usai, S. (2003), A least squares database approach for SAR interferometric data, *IEEE Trans. Geosci. Remote Sens.*, *41*, 753–760.

Wang, H. F. (2000), *Theory of Linear Poroelasticity: With Applications to Geomechanics*, 287 pp., Princeton Univ. Press, Princeton, N. J.

Wicks, C., Jr., W. Thatcher, and D. Dzurisin (1998), Migration of fluids beneath Yellowstone Caldera inferred from satellite radar interferometry, *Science*, *282*, 458–462.

Williams, C. A., and G. Wadge (1998), The effects of topography on magma reservoir deformation models: Application to Mt. Etna and radar interferometry, *Geophys. Res. Lett.*, *25*, 1549–1552.

Zebker, H., P. Rosen, and S. Hensley (1997), Atmospheric effects in interferometric synthetic aperture radar surface deformation and topographic maps, *J. Geophys. Res.*, *102*, 7547–7563.

Zebker, H., F. Amelung, and S. Jonsson (2000), Remote sensing of volcano surface and internal processing using radar interferometry, in *Remote Sensing of Active Volcanism*, *Geophys. Monogr. Ser.*, vol. 116, edited by P. Mouginis-Mark et al., 179–205, AGU, Washington, D. C.

D. Dzurisin, U.S. Geological Survey, David A. Johnston Cascades Volcano Observatory, 1300 SE Cardinal Court, Building 10, Suite 100, Vancouver, WA 98683-9589, USA. (dzurisin@usgs.gov)

Z. Lu and T. Masterlark, Science Applications International Corporation, National Center for Earth Resources Observation and Research, U.S. Geological Survey, 47914 252nd Street, Sioux Falls, SD 57198, USA. (lu@usgs.gov; masterlark@usgs.gov)